Exploring failure modes of alumina scales on FeCrAl and FeNiCrAl alloys in a nitriding environment

Downloaded from: https://research.chalmers.se, 2026-04-04 16:33 UTC

Citation for the original published paper (version of record):

Mortazavi, A., Esmaily, M., Geers, C. et al (2020). Exploring failure modes of alumina scales on FeCrAl and FeNiCrAl alloys in a nitriding environment. Acta Materialia, 201: 131-146. http://dx.doi.org/10.1016/j.actamat.2020.09.058

N.B. When citing this work, cite the original published paper.

research.chalmers.se offers the possibility of retrieving research publications produced at Chalmers University of Technology. It covers all kind of research output: articles, dissertations, conference papers, reports etc. since 2004. research.chalmers.se is administrated and maintained by Chalmers Library

(article starts on next page)

Acta Materialia 201 (2020) 131–146

Contents lists available at ScienceDirect

Acta Materialia

journal homepage: www.elsevier.com/locate/actamat

Exploring failure modes of alumina scales on FeCrAl and FeNiCrAl alloys in a nitriding environment

A.N. Mortazavi[a,*], M. Esmaily[b], C. Geers[c], N. Birbilis[d], Jan-Erik Svensson[c], M. Halvarsson[e], D. Chandrasekaran[f], L.G. Johansson[c]

[a] School of Engineering and Applied Sciences, Harvard University, Cambridge, USA
[b] Department of Materials Science and Engineering, Massachusetts Institute of Technology, Cambridge, United States
[c] Department of Chemistry and Chemical Engineering, Chalmers University of Technology, Gothenburg, Sweden
[d] College of Engineering and Computer Science, The Australian National University, Canberra, Australia
[e] Department of Physics, Chalmers University of Technology, Gothenburg, Sweden
[f] Kanthal AB, Hallstahammar, Sweden

ARTICLE INFO

Article history:
Received 9 May 2020
Revised 15 September 2020
Accepted 17 September 2020
Available online 30 September 2020

Keywords:
High temperature oxidation
Nitridation
Alumina scale failure
Crystallographic orientation
Reactive elements

ABSTRACT

Two high-temperature FeCrAl and FeNiCrAl alloys were exposed in a strongly nitriding environment at 900 °C and the morphology of nitridation was studied. Quasi-in-situ experiments revealed that nitridation started at specific surface sites directly related to the alloy microstructure where the alumina scale was permeable to nitrogen. FeCrAl alloy grains with (112) orientation formed outward-growing alumina scales and were susceptible to nitridation. Outward-growing scales and substrate nitridation was also observed at chromium carbide precipitates in the FeNiCrAl alloy. Both alloys suffered nitridation at reactive element-rich (Y and Zr) inclusions larger than a certain critical size. The latter type of attack is caused by cracks and pores in the scale. The findings open new avenues of research for developing the next generation of high temperature alloys with superior properties.

© 2020 Acta Materialia Inc. Published by Elsevier Ltd.
This is an open access article under the CC BY-NC-ND license
(http://creativecommons.org/licenses/by-nc-nd/4.0/)

1. Introduction

The ability of high-temperature alloys to resist corrosion due to reactions with, e.g., O, N, C, and S, relies on the formation of a protective oxide layer, i.e., the oxide scale, which separates the alloy from the environment. Most high-temperature alloys are designed to form chromia (Cr_2O_3) or alumina (Al_2O_3) scales. In air and at temperatures <1000°C, chromia-forming alloys are often used. At higher temperatures, high-temperature alloys forming protective alumina scales, for example Fe-based (FeCrAls) [1–3], Ni-based (NiCrAls) [1–6], and Co-based (CoCrAls) [1,3], are preferred. This is because α-Al_2O_3 scales grow very slowly and because alumina is thermodynamically quite stable and chemically inert [7–12]. To improve the protective properties of the alumina scale, especially its adhesion, small amounts of certain "reactive elements" (REs) such as Y and Zr are added to the alloys. RE alloying increases the lifetime of components by several orders of magnitude [13–16].

Low-oxygen-activity environments which contain other oxidants, such as N and C, are very demanding from a corrosion point of view because of the difficulty in forming and maintaining a protective oxide scale. Scale failure can result in rapid nitridation or carburization. One example is the $N_2 + H_2$ environments used in heat treatment furnaces, industrial processing, and sintering operations, where construction materials tend to suffer nitridation. Although chromia-forming nickel-based alloys are presently the industry standard for such applications, nitridation issues are far from being solved, especially when the water content is low and temperature is high (>1000°C) [8]. Indeed, chromia scales appear to be inherently permeable to nitrogen, hence providing poor protection in such demanding environments [17].

Alumina-forming alloys are used less often in high-temperature nitriding environments. One potential issue is AlN precipitation, which causes the remaining alloy to be depleted in aluminum, thus effectively removing the alloy component required to form the protective oxide scale. However, in a recent work on the nitridation of FeCrAl (Kanthal APMT) in a very dry $N_2 + H_2$ environment at 900°C, Geers et al. [17] reported that the alloy showed a promising ability to resist nitridation. Thus, nitridation was reported to be

* Corresponding author
E-mail address: nmortazavi@seas.harvard.edu (A.N. Mortazavi).

https://doi.org/10.1016/j.actamat.2020.09.058
1359-6454/© 2020 Acta Materialia Inc. Published by Elsevier Ltd. This is an open access article under the CC BY-NC-ND license
(http://creativecommons.org/licenses/by-nc-nd/4.0/)

restricted to relatively small "pockets" at the surface, with most of the alloy being unaffected after four weeks of cyclic exposure. This implies that the thermally grown alumina scale has an inherent ability to protect against nitrogen ingress into the alloy and that the nitridation can be attributed to imperfections in the alumina layer that allow nitrogen to circumvent it. This suggest that if such scale imperfections can be avoided, alumina-forming alloys can be superior to chromia scales in a nitriding environment.

The main focus of this paper is to describe how alumina scales fail in a nitriding environment and why they do not heal again. The idea is that detailed knowledge of the reasons behind the scale failure will enable the development of new alumina-forming alloys with better ability to resist nitridation. To this end, failure modes of alumina scales formed on two alloys (FeCrAl Kanthal APMT and FeNiCrAl Nikrothal PM58) were investigated in a low-oxygen-activity, strongly nitriding environment. The two alloys under investigation are among the best performing of all alumina formers with respect to high-temperature oxidation in air and they are not prone to internal oxidation [2]. Nitridation is relatively slow at the experimental temperature (900°C), which enables a detailed investigation of its initial stages. Quasi-in-situ experiments were carried out to correlate oxidation behavior with the size and crystallographic orientation of the alloy grains, with refractory carbide inclusions and with RE-rich particles in the alloys.

2. Experimental

2.1. Materials

The alloys investigated were Kanthal APMT and Nikrothal PM58, (see the chemical composition in Table 1). Both materials are oxide dispersion-strengthened alumina-forming alloys with superior high-temperature properties and contain a high number density of RE–rich nanoparticles. Kanthal APMT is a ferritic FeCrAl alloy designed for use at temperatures of up to 1300°C. Nikrothal PM58 is an austenitic FeNiCrAl alloy designed for use up to 1200°C in air. The alloys were fabricated by Kanthal AB. The production of both alloys comprises melting of the raw materials, powder production via gas atomization, hot isostatic pressing, and hot processing followed by cold forming [18].

2.2. Nitriding exposures

The test coupons (dimensions 2.0 × 15.0 × 15.0 mm^3) were cut from strip material and ground on SiC paper to 4000 grit. The coupons were then polished using 1 μm diamond suspension and thoroughly cleaned before exposure. In the quasi-in-situ experiments the samples were polished using 0.25 µm diamond suspension.

The samples were exposed to a strongly nitriding environment comprising 95% N_2 + 5% H_2/D_2 + ~35 ppm H_2O/D_2O at 900°C up to one month. Details of the exposures can be found in [19]. The exposure setup comprised a horizontal three-zone tube furnace fitted with a 1.00-m tube made from sintered corundum with an inner diameter of 45 mm. The tube was purged with a stream of N_2 + H_2 gas for several hours before the experiment. The water content in the gas was estimated on the basis of complete conversion into H_2O of the traces of O_2 detected in the nitrogen stream. The O_2 measurements were done with an oxygen sensor Rapidox 2100ZF equipment.

Table 1
Nominal chemical composition (wt. %) of the alloys.

	Fe	Ni	Cr	Al	Mo	Si	Other
Kanthal APMT™	Balance	–	21	5	3	–	Y, Zr, Hf
Nikrothal PM58™	18	Balance	19	5	–	0.4	Y, Zr, Hf

2.3. Postexposure analysis

An FEI Quanta 200 environmental scanning electron microscopy (ESEM) equipped with a field emission gun (FEG) and an Oxford Inca energy-dispersive X-ray spectroscopy (EDXS) microanalysis system, and a LEO Ultra 55 FEG-SEM equipped with an HKL Channel 5 electron backscatter diffraction (EBSD) system were used to study both the microstructure of the uncorroded samples and the corrosion morphology after the exposures. The SEMs were operated at 20 kV during the EBSD examinations and at 10–15 kV during the EDXS analysis. An FEI Versa 3D combined focused ion beam/SEM (FIB/SEM) workstation was used to produce cross sections and thin foils from the oxide scales and subjacent metal. A pre-tilted (45°) sample holder was used for the SEM-EDXS analysis of the FIB-prepared cross sections. Quasi-in-situ experiments were carried out using FIB milling and extensive microscopy before and after the exposures. In addition, a Leica EM TIC 3X broad ion beam milling (BIB) system was used to make large cross sections (up to ~1-1.5 mm wide and several hundred microns deep).

The FIB-prepared thin foils were studied by scanning transmission electron microscopy (STEM) in an FEI Titan 80-300 TEM-STEM system equipped with an Oxford Instruments EDXS detector and an FEG. STEM images were captured using bright field (BF) and high-angle annular dark field (HAADF) detectors. The SEM-based transmission Kikuchi diffraction (TKD) method was used to identify the crystalline compounds that formed during exposures using a home-built TKD stage designed for oxidation studies [20]. Statistical analysis was carried out using SEM and STEM images processed by Adobe Photoshop CS4 and Image Pro-Plus. Time-of-flight secondary ion mass spectrometry (ToF-SIMS) analysis was conducted using a TOF.SIMS 5 instrument equipped with a 25-keV Bi_3^+ cluster ion gun as the primary ion source and a 10-keV Cs^+ ion source for sputtering and etching. More details of the TOF-SIMS analysis can be found elsewhere [19].

3. Results

3.1. Alloy microstructure

Kanthal APMT is a FeCrAl alloy with a fine microstructure with an average grain size of 8.8 µm (Fig. 1*a* and *b*) and is very weakly textured. The microstructure is quite stable during service because of a homogeneous high-density distribution of RE-rich nanosized refractory inclusions containing oxygen, carbon, and nitrogen [18] (a representative STEM image showing the inclusions in this alloy is provided in Fig. 1*c*). The refractory inclusions do not coarsen upon extended exposure at high temperature [18]. The results of the statistical analysis of the SEM and STEM micrographs revealed that the RE-rich (mainly containing Y and Zr) particles were mainly in the 10–300 nm, with the RE particles being omnipresent in the alloy microstructure (see Fig. 1d). A small number of larger (>300 nm) RE-rich particles were also present. It has been shown that the RE microalloying additions are present as discrete particles and not as solute atoms [19]. Nikrothal PM58 is an austenitic NiCrFeAl alloy with excellent high-temperature oxidation properties, and similar to the FeCrAl alloy, it has a high density of RE-rich particles [2]. The chemical composition and microstructure of the two alloys are fully optimized with respect to oxidation properties at elevated temperatures.

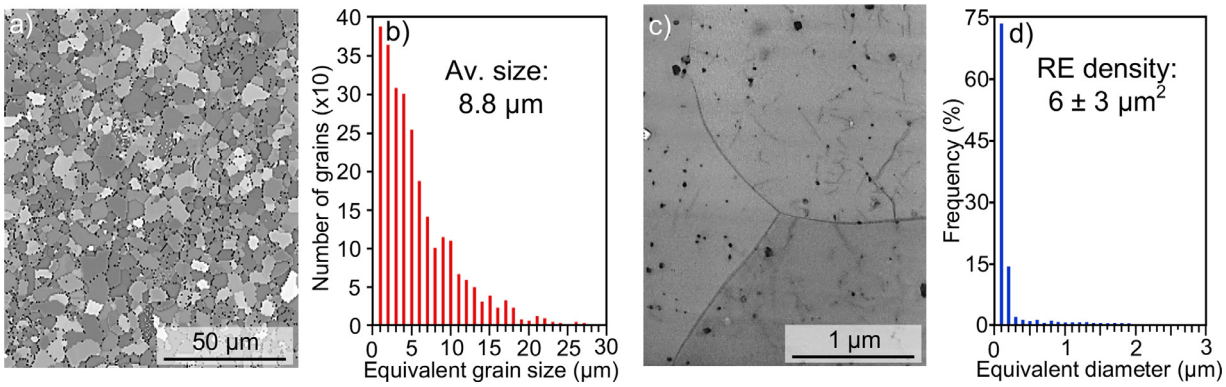

Fig. 1. Microstructure of the FeCrAl alloy. (*a*) EBSD band contrast map showing the alloy grain structure, (*b*) grain size distribution (from EBSD analysis), (*c*) STEM micrograph showing the fine distribution of nanosized inclusions, and (*d*) size distribution of RE-rich particles.

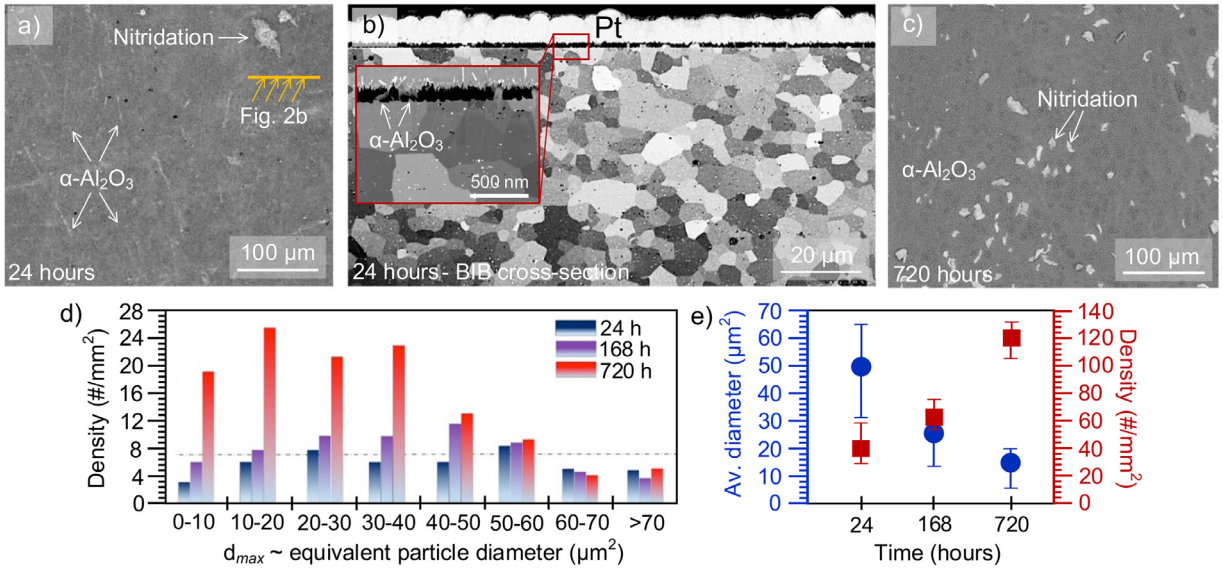

Fig. 2. Overview of nitridation of the FeCrAl alloy. (*a–c*) SEM backscattered electron images showing plan-view images and a BIB-prepared cross section of the alloy after 24 and 720 h of exposure. (*d* and *e*) Statistical analysis describing the size and distribution of the nitrided zones at the alloy surface in an area of 2 × 2 mm².

3.2. Alloy nitridation

An overview of the corrosion morphology of the FeCrAl alloy after 24 and 720 h in the nitriding environment is given in Fig. 2*a–c*. As can be seen in Fig. 2b, most of the surface was covered by a smooth and protective alumina layer, i.e., the “base alumina”. Scattered nitrided zones of different sizes were observed irrespective of exposure time. In many cases, the shape of the nitrided zones was roughly semi-spherical. The results of the statistical analysis (Fig. 2*d* and *e*) showed that, although the number of nitrided zones increased roughly four times between 24 and 720 h, the average diameter decreased (Fig. 2*e*). The changing size distribution as a function of exposure time implies that the nitrided zones do not grow laterally and that the “new” nitrided zones appearing are relatively small. A comparison of the cross sections after 24, 168, and 720 h showed very little thickness growth of the base alumina layer.

Cross-sectional analysis of the FIB-prepared specimens after 24 and 720 h of nitridation at 900°C are given in Fig. 3*a* and *b*, respectively. The nitridation products designated in Fig. 3 were analysed and identified experimentally by EDXS and TKD. Elemental mapping shows that the nitrided zones were lined with an almost continuous layer of AlN precipitates [8,17,21,22], which separated them from the remaining sound alloy. Needle-like AlN precipitates were also found within the nitrided zones, intermingled with equiaxed Cr_2N precipitates [8,17,21]. CrN particles were detected in the top part of the nitrided zone, just beneath the surface. The nitride precipitates formed both on the alloy grain boundaries (GBs) and within the grains. EDXS elemental maps revealed that the nitrided zone was covered by a thin alumina scale (see the Al map in Fig. 3*b*). The morphology of the nitridation of the FeNiCrAl alloy was similar to that of the FeCrAl alloy. A cross section of a typical nitrided zone in the FeNiCrAl alloy (168 h) is shown in Fig. 3*c*.

The Al content in the remaining metal within the nitrided zone was below the detection limit of the SEM-EDXS analysis (< 0.1 at. %). Considering the thermodynamic stability of AlN compared with that of chromium nitrides [17,23], the presence of Cr_2N and CrN implies that the remaining alloy in the pocket is essentially free from Al. Because of Al depletion, the remaining metal in the nitrided zones reacts with the traces of water in the gas to form a chromia scale. The small chromia islands observed on top of the nitrided zone after 24 h (as identified by SEM-EDXS; see Fig. 3*a*) are attributed to this process. With time, the surface of the nitrided zones becomes completely covered by chromia (see Fig. 3*b*) after 720 h.

Although the nitrided zones do not appear to grow laterally with increasing exposure time (Fig. 2*d*), several FIB cross sections prepared after 24, 168, and 720 h showed that the nitrided zones

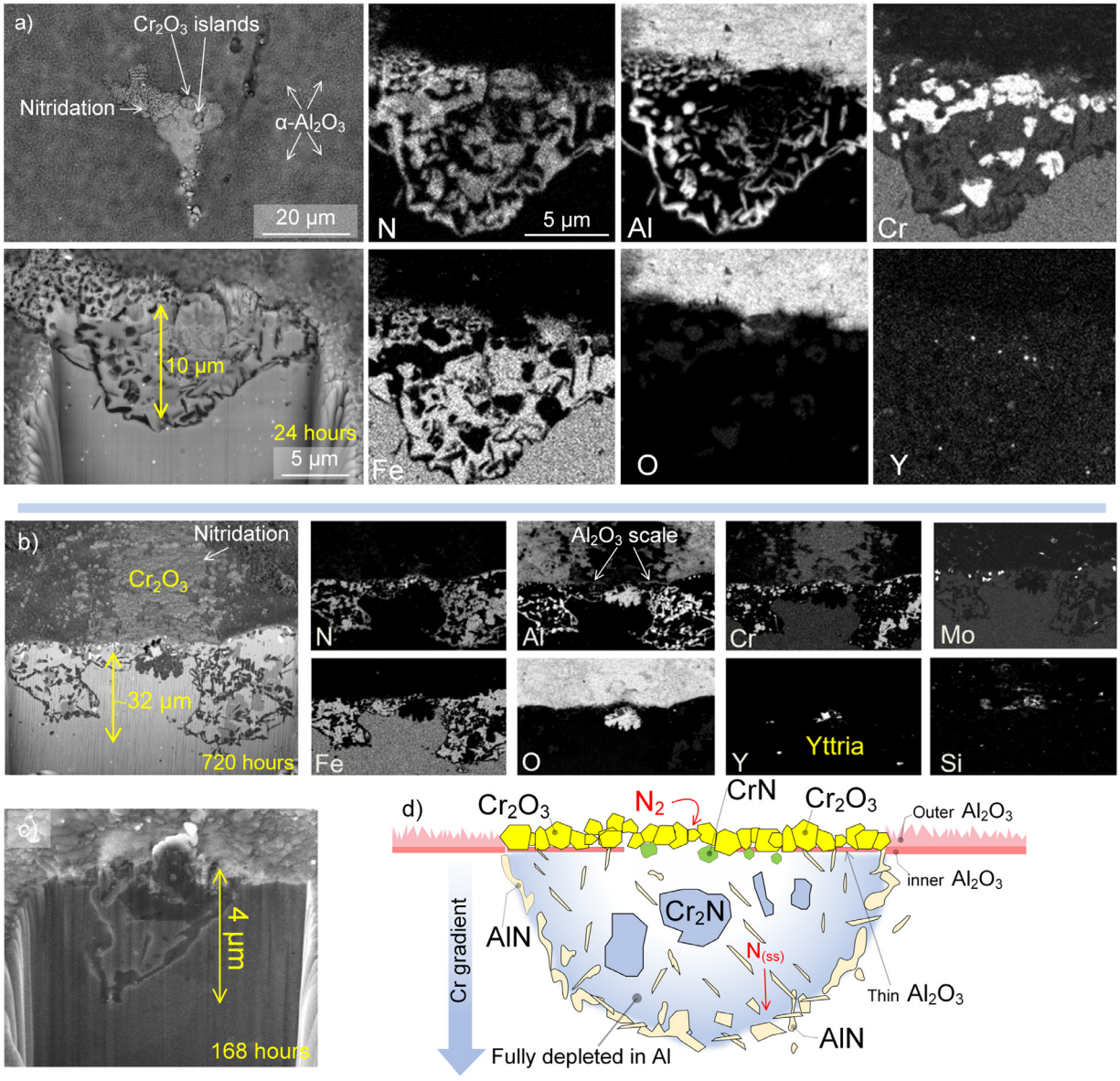

Fig. 3. SEM-FIB-EDXS cross-sectional analysis of nitrided zones in the FeCrAl alloy and the FeNiCrAl alloy after exposure in $H_2 + N_2$ + ~35 ppm H_2O at 900°C (*a* and *b*) Representative areas revealing the morphology and chemistry of the nitrided zones formed after 24 and 720 h, respectively; (*c*) a typical nitrided zone in the FeNiCrAl alloy observed after 168 h of exposure; and (*d*) schematic illustration of the morphology of the nitrided zones.

grow inward, into the alloy, during the exposure. The continued inward growth of the nitrided zones is in accordance with a recent study reporting that chromia scales on Al-bearing alloys are permeable to nitrogen [17]. The measured Cr concentration in the remaining alloy after 720 h of nitridation was 5–12 wt.%, decreasing toward the sample/gas interface.

To investigate the morphology and chemistry of nitridation in detail, several small nitrided zones on the FeCrAl alloy surface were selected and investigated at high resolution using FIB-STEM-EDXS. Figs. 4 and 5 show two representative examples from a sample exposed for 24 h. The SEM surface analysis in Fig. 4*a* shows the presence of two equiaxed particles (P1 and P2) on top of the nitrided zone. Using FIB, a thin foil was prepared, which included both the particles on the surface and the nitrided substrate (Fig. 4*b*–*e*). The composition of the nitrided zone (Fig. 4*b*) was similar to that of the larger nitrided zones in Fig. 3. Analogous with Fig. 3, the base oxide consisted of α-alumina. Submicron cracks were also observed in the alumina layer at the periphery of the nitrided zone (see the arrow in Fig. 4*c*).

Table 2
STEM-EDXS point analysis (in at. %) from two areas designated in Fig. 4d.

Area/element	Fe	Cr	Mo	Si	Al
P2	92.3	6.04	0.15	1.40	-
M3	91.7	5.65	0.16	1.88	-

Analysis of the two particles (P1 and P2) on the scale surface by STEM-EDXS (Fig. 4*d* and *e*) showed that P2 consisted of iron-rich metal with small amounts of SiO_2 on its surface while P1 consisted of Mo-containing CrN (elemental maps in Fig. 4*e*). STEM-EDXS analysis revealed that the chemical composition of the metal particle P2 was similar to the remaining metal immediately below the surface (P2 and M3 in Fig. 4*d* and the corresponding EDXS values in Table 2).

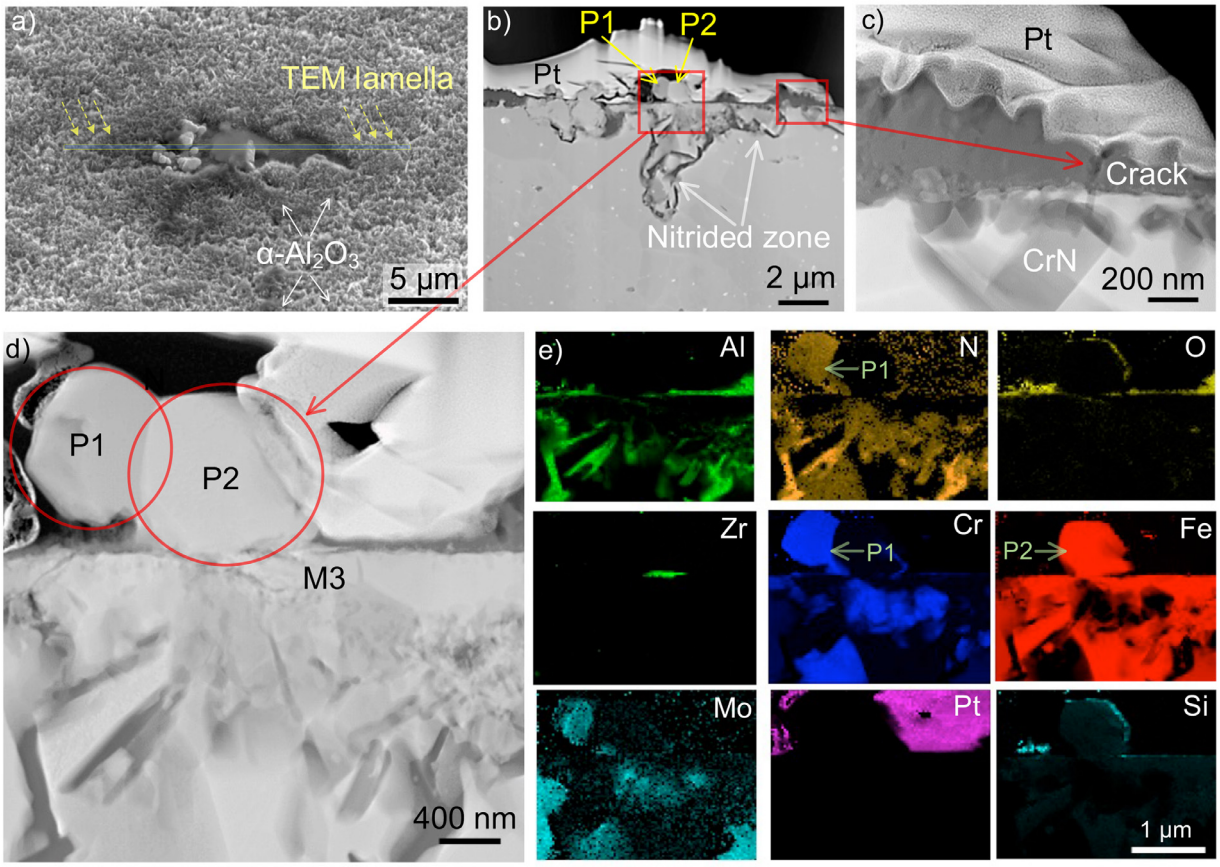

Fig. 4. Detailed morphology of a a small nitrided zone in the FeCrAl alloy after 24 h exposure to N_2 + H_2 + ~35 ppm H_2O at 900°C. (*a*) SEM image of the surface; (*b*) STEM HAADF image showing a cross section at the position indicated in Fig. 3*a*; (*c*) a higher magnification image showing a sub-micron crack in the scale on top of the nitrided zone; (*d* and *e*) STEM-EDXS analysis of two equiaxed particles P1 and P2 on top of the nitrided zone. The STEM-EDXS analysis revealed that P2 had similar chemical composition as the remaining metal in the substrate (M3) (see the compositions in Table 2).

Another representative example of a nitrided zone in the FeCrAl alloy (24 h exposure) is shown in Fig. 5. It is relatively small and is similar to the nitrided zones in Figs. 3 and 4. The surface of the nitrided zone is covered by a very thin alumina layer (compare the thicker scale on the sound alloy to the left in Fig. 5*a*). An inspection of Fig. 5*b* and *c* shows that the scale on the nitrided zone has a three-layer structure with a total thickness of about 100 nm. It features a middle layer consisting of remaining metal, which is sandwiched between a top alumina layer and a discontinuous bottom AlN layer. The alumina layer contains defects and cracks (Fig. 5*c*) and incorporates CrN and Cr_2N particles.

The thermodynamics of the nitridation process is illustrated in Fig. 6. The alloy composition in the calculations corresponds to that of the FeCrAl alloy. According to Fig. 6*a*, the traces of H_2O present in the exposure gas (about 35 ppm) are sufficient to stabilize Cr_2O_3 on the alloy surface. This is in agreement with the observation of Cr_2O_3 on the surface of the nitrided zones (as islands (Fig. 3*a*) and as a continuous layer; see the Al map in Fig. 3*b* and in refs. [17,19]). A calculated phase stability diagram for alloy nitridation is shown in Fig. 6*b*. It illustrates the well-known stabilization of austenite by N [24–28], the remaining alloy in the nitrided zones going from ferritic to austenitic after completed AlN precipitation. The star in Fig. 6*b* corresponds to saturation of the alloy with respect to N (95% N_2 (*g*)).

The corresponding equilibrium solid is a mixture of AlN, CrN and austenite, the Cr content in the remaining metal being 2.6 wt. %. The observation (by SEM-EDXS; see Fig. 3) that Cr_2N is present throughout the nitrided zones irrespective of exposure time (24, 168, and 720 h), thus shows that the nitrided zones are not saturated with N. Accordingly, the lowest Cr content measured in the remaining alloy was approximately 3.9 wt. %. Moreover, the observation that CrN was only detected close to the gas interface (see *e.g.*, Figs. 3 and 5*c*) indicates the presence of a nitrogen gradient. Indeed, the presence of such a gradient is in accordance with the observation that the nitrided zones continue to grow inward during the exposures.

3.3. Investigation of the failure modes of the alumina scale

The main focus of this paper is to describe the imperfections in the alumina scale, which allow nitrogen to penetrate into the alloy, and to explore how these imperfections appear and why they do not heal. At this point, it may be noted that the corroded samples not only exhibit the typical nitrided zones shown in Figs. 2–5, but also show evidence for nitridation on a smaller scale. These limited attacks are considered to correspond to early stages of nitridation, which later develop into the characteristic nitrided zones. In order to explain why a protective alumina scale fails to form at certain sites it is desirable to study the alloy surface, both before and after the corrosion experiment, in a way that allows individual microstructural features to be identified and related to a certain corrosion behavior. Moreover, it is important that the number of investigated microstructural features is large enough for the results to be statistically significant.

To achieve this, “marker exposures” were performed involving relatively large areas. First, a region of interest (ROI) was delineated on the unexposed sample surface using cross marks prepared by FIB (see Fig. 7*a*). These markings were then used to iden-

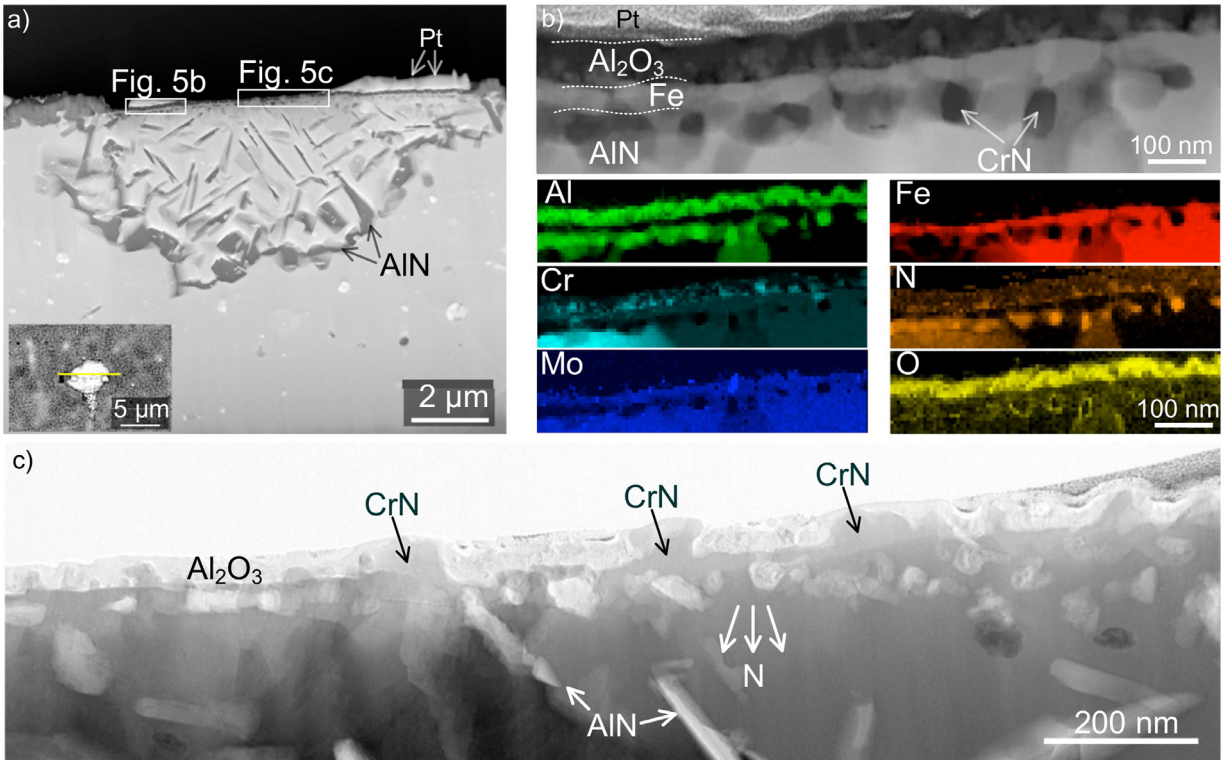

Fig. 5. Detailed morphology of a typical nitrided zone in the FeCrAl alloy (*a*) STEM HAADF micrograph of a cross section of the nitrided zone shown in the SEM image insert; (*b*) STEM-HAADF-EDXS analysis of the area indicated in (*a*). Note the layered scale, comprising a Fe-rich layer sandwiched between a top alumina layer and a bottom AlN layer; and (*c*) STEM BF micrograph of the area indicated in (*a*) showing the defective nature of the alumina layer, which incorporates chromium nitride particles. (Exposure to H_2 + N_2 + ~35 ppm H_2O for 24 h at 900°C).

tify all alloy grains in the ROI by defining their positions. In the example in Fig. 7, nearly 1800 grains were identified in this way. Subsequently, the microstructure (*e.g.,* grain size and chemical composition) and crystallographic orientation of all grains in the ROI were characterized using SEM-EDXS and EBSD mapping. After these extensive preparations, the sample (with the ROI) was exposed to the nitriding environment (95% N_2 + 5% H_2 + ~35 ppm H_2O at 900°C) for 168 h.

After the exposure, all alloy grains in the ROI were again identified and subsequently analyzed with respect to the microstructure of oxidation and nitridation (see for instance Figs. 7–9). This allowed the identification of all alloy grains in the ROI both before and after the exposure, so that the corrosion morphology of each grain could be correlated with its crystallographic orientation and original microstructure. Investigating the oxidation performance of individual grains and correlating the local oxidation morphology with the SEM-EDXS-EBSD microstructural analysis before exposure, showed that both the *crystallographic orientation of the grains* and the presence of *precipitates* strongly affected the "local" oxidation performance of the alloy. In contrast, no effect of grain size was seen. By this procedure three "alumina scale failure modes" were distinguished, which all resulted in nitridation of the alloy substrate and generation of the typical morphologies described in Figs. 2–5.

3.4. Failure mode I: Orientation-dependent oxidation and nitridation

After the exposure, the ROI exhibited four distinctive morphologies: (*i*) the smooth base alumina covering >95% of the surface, being similar to the example shown in Fig. 2*b*, (*ii*) areas covered by "rough" alumina, corresponding to the darker isolated regions in Fig. 7*b* and *c*, (*iii*) areas affected by nitridation, corresponding to the bright features in Fig. 7*b*, and (*iv*) areas showing signs of both nitridation and a relatively rough alumina (*i.e.*, a combination of (*iii*) and (*ii*)) (Fig. 7*c*). After the exposure, all grains in the ROI that exhibited a dark contrast (morphology *ii* = rough alumina) and a bright contrast (morphology *iii* = nitrided substrate) were analyzed by FIB-SEM-EDXS. Analysis of the bright areas showed that they always coincided with the nitrided zones, *i.e.*, cross-sectional analysis verified that these grains had suffered nitridation of the type illustrated in Figs. 4 and 5.

Several examples of such areas are shown in Fig. 7*d* and *e* (the four bright contrast grains, representing nitrided zones, are designated as G_{N1}–G_{N4}, respectively, whereas the 18 grains representing the rough alumina are designated as G1–G18, respectively). The crystallographic orientation of all 22 grains is illustrated by the EBSD map in Fig. 7*e* and by the inverse pole figure representation in Fig. 7*f*. The same color codes for the grain orientations are used in the EBSD map (Fig. 7*e*) and in the inverse pole figure (Fig. 7*f*). It turned out that the occurrence of bright regions (morphology *iii*), *i.e.*, grain nitridation, depended on crystallographic orientation. Thus, an inspection of Fig. 7*d–f* shows that the four bright (nitrided) grains had an orientation close to (112). The dark grains (morphology *ii*) corresponding to a rough alumina *but with no nitridation*, also showed a strong tendency to be (112) oriented, (<5° angular deviation from the (112) plane, *i.e.* $\beta_{(112)}$ = 0°–5°). To some extent, morphology *ii* was also promoted on grains with orientations between (112) and (111). In contrast, grains exhibiting all other orientations did not develop a rough alumina layer, nor did they suffer nitridation, their alumina scales being smooth and apparently impermeable to nitrogen.

The atomic arrangement of the four bcc planes indicated in the pole figure map is shown in Fig. 7*g*. The atomic planar density (= number of atoms/unit area) is highest for the (101) plane ($0.27/R^2$), second highest for the (001) plane ($0.19/R^2$), and lowest for the (112) plane ($0.10/R^2$), where R is the ion radius. Thus, the grain

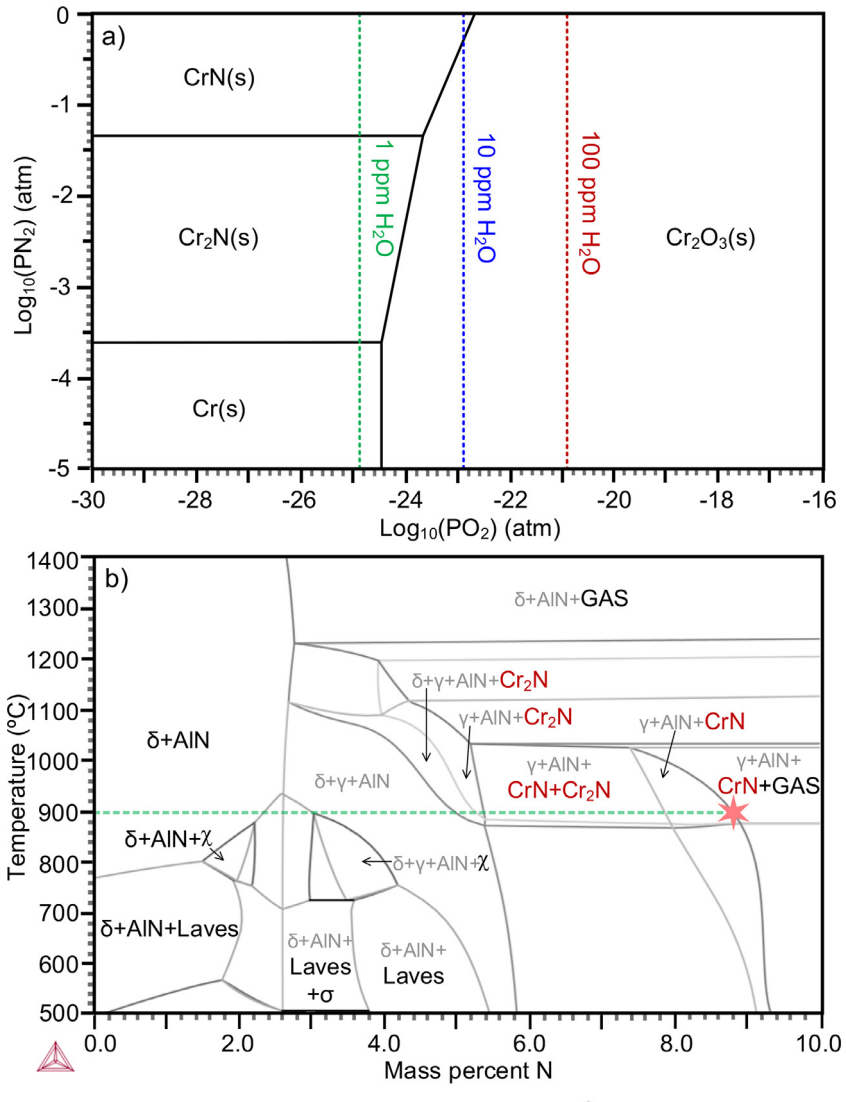

Fig. 6. Stability diagrams calculated using ThermoCalc® - Database: TCFE10. (*a*) Cr–N–O stability diagram at 900°C. The vertical dotted lines correspond to different concentrations of H_2O in the nitriding gas (calculated based on [29]); and (*b*) nitridation of an alloy containing 69Fe, 23Cr, 5Al, and 3Mo (wt. %), corresponding to the composition of the FeCrAl alloy under investigation here.

surfaces exhibiting the lowest atomic density (112-oriented; purple in Fig. 7*e*) are also most prone, both to form a rough alumina scale and to suffer nitridation.

To elucidate the microstructure and the properties of the rough alumina scale formed on the (112) facets, a dedicated microscopy study was performed. Representative STEM images are in Fig. 8. A typical (112)-oriented grain covered by a thick and rough alumina scale is in Fig. 8*a*. In contrast, the alumina layer on the neighbouring (101)-oriented grain is relatively thin and smooth. This is in accordance with Fig. 7, showing that the crystallographic orientation of the grains has a major effect on the alumina layer morphology. High-magnification STEM images from the boxed areas in Fig. 8*a* are shown in Fig. 8*b* and *c*. It was evident that the alumina scales forming on grain surfaces other than those of (112) and (111) were free of defects and exhibited both inward- and outward-grown parts. In Fig. 8*b*, the original alloy surface corresponds to the row of bright nanoparticles in the bottom part of the alumina layer. The nanoparticles consist of Cr^{3+}- rich oxide and are remnants from the transient oxidation stage [30].

In contrast, the alumina forming on the (112)-oriented grains is rough and contains a high fraction of voids, both at the alloy/oxide interface and within the scale (see for example Figs. 8*c* and *d*). Moreover, the (112)-oriented grains tended not to form an inward-grown alumina layer (Fig. 8*c*). A nano-sized Zr-rich oxide particle within the alumina layer on a (112)-oriented grain is presented in Fig. 8*d*. It corresponds to the high density of nanosized RE particles present on the alloy surface before the exposure (c.f., Fig. 1*c* and *d*). Detailed microscopy indicated that the alumina layer that formed in the vicinity of the Zr enrichment was nanocrystalline and free from defects. Notably, while the alumina scale formed on the (112) oriented grain was otherwise only outward-grown, the alumina in the vicinity of the Zr-rich area was inward-grown (this is further discussed below in the subsection *Failure Mode III*).

3.5. Failure mode II: Chromium carbide precipitates

Microstructural characterization of the FeNiCrAl alloy showed that it contains a high density of chromium-rich carbide particles. Carbides are widely used for precipitation strengthening of high-

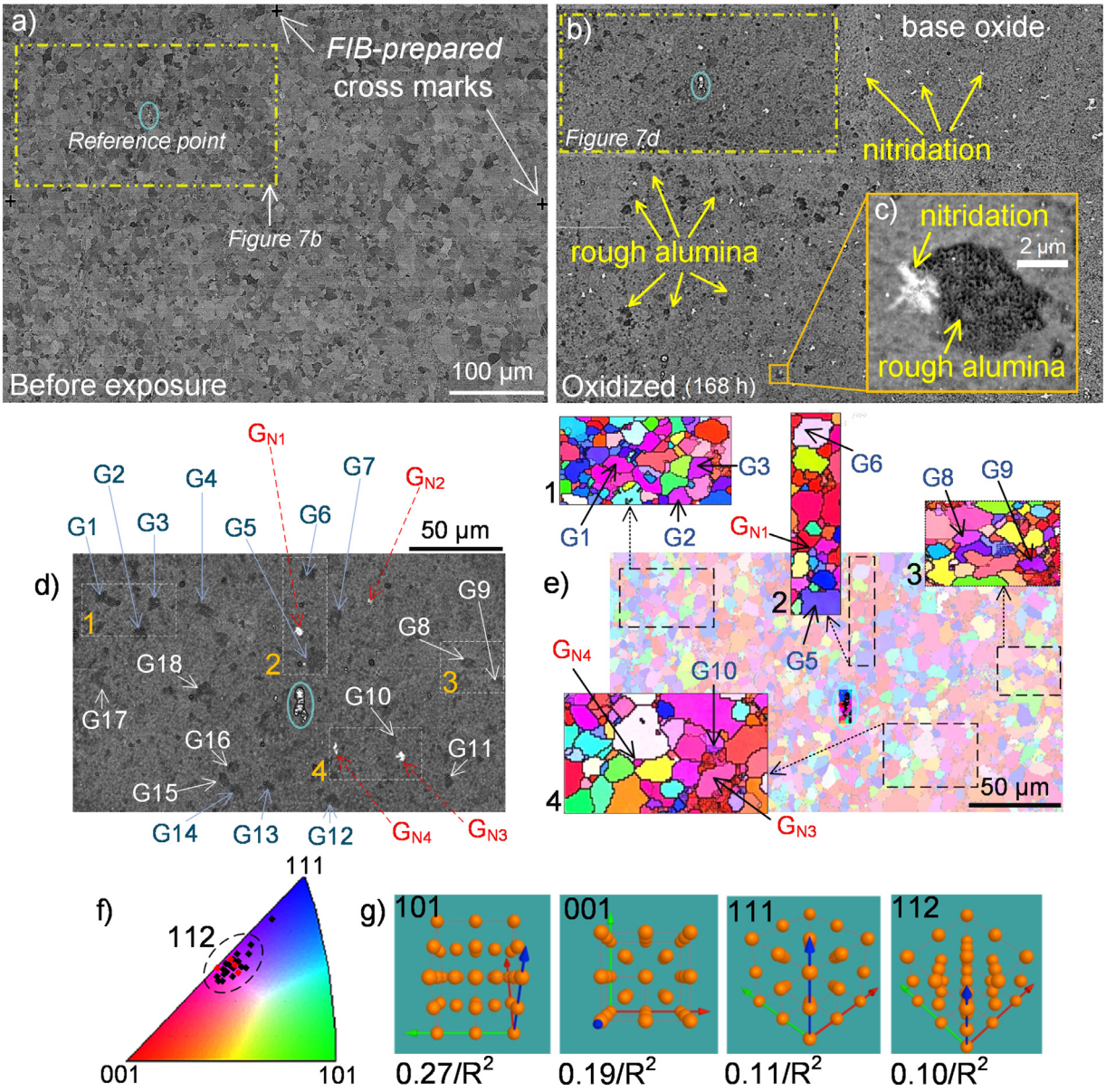

Fig. 7. Quasi-in-situ investigation of the influence of crystallographic orientation on nitridation of the FeCrAl alloy (*a*) SEM backscattered electron image showing the region of interest (ROI) and the grain structure before the exposure. FIB-prepared cross marks were used to locate the ROI and all individual grains within it, both before and after the corrosion exposure. (*b*) SEM image showing the same region after 168 h of exposure to N_2 + H_2 (+ ~35 ppm H_2O) at 900°C, (*c*) a tilted SEM image showing two common surface features; nitridation (*iii*) and rough alumina (*ii*), (*d* and *e*) SEM image showing the region of interest (= the boxed area in (*b*)) after the exposure and an EBSD map of the same area before the exposure, showing the correlation of grain orientation and corrosion morphology, (*f*) color-coded inverse pole figure map along the surface normal direction indicating the crystallographic orientation of the grains highlighted in (*d*) and (*e*). (*g*) Atomic planar density (= number of atoms/unit area) for bcc surfaces with different crystallographic orientations. Note (1): G1, G2, … G18 are grains covered by rough alumina (compared to the base oxide). Note (2): G_{N1}, G_{N2}, G_{N3}, and G_{N4} are grains that both exhibited rough alumina *and* suffered nitridation. (For interpretation of colours, the reader is referred to the web version of the article.)

temperature alloys [31]. Before the oxidation exposure, the exact position of carbide particles at the surface were identified. An area of interest was then defined using FIB-milled markings, similar to the quasi-*in-situ* experiment described above (Figs. 7 and 8). Subsequently, the sample was exposed to the strongly nitriding environment (5% H_2 + 95% N_2 + ~35ppm H_2O at 900°C, 168 h). After the exposure, FIB-prepared thin foils were made for characterization by FIB-STEM-EDXS.

The STEM micrograph in Fig. 9*a* shows an alloy cross section which includes a micron-size Cr-rich carbide ($M_{23}C_6$, as identified by EDXS) particle after exposure to the nitriding environment. An inspection of the N and Al maps in Fig. 9*b* shows clear evidence for nitride formation at the carbide particle/alloy interface, showing that the chromium-rich carbide inclusions create weak spots in the alumina scale that allow nitrogen to penetrate to the alloy substrate. As noted above, this is an example of early nitridation that later develops into the characteristic nitrided zones shown *e.g.*, in Fig. 2.

Although most of the sample surface is covered by a relatively smooth alumina scale (*i.e.*, the base alumina layer) with a thickness of 300 ± 40 nm, the oxide scale that formed in the vicinity of the carbide particle is rough and thicker (2000 ± 500 nm). A TKD investigation showed, as expected, that the base alumina layer consists of α-Al_2O_3 (area 1 in Fig. 9*a*). In contrast, the rough oxide scale formed at the chromium carbide particle is made up of two phases. Part of it consists of α-Al_2O_3 (area 2 in Fig. 9*a*), whereas

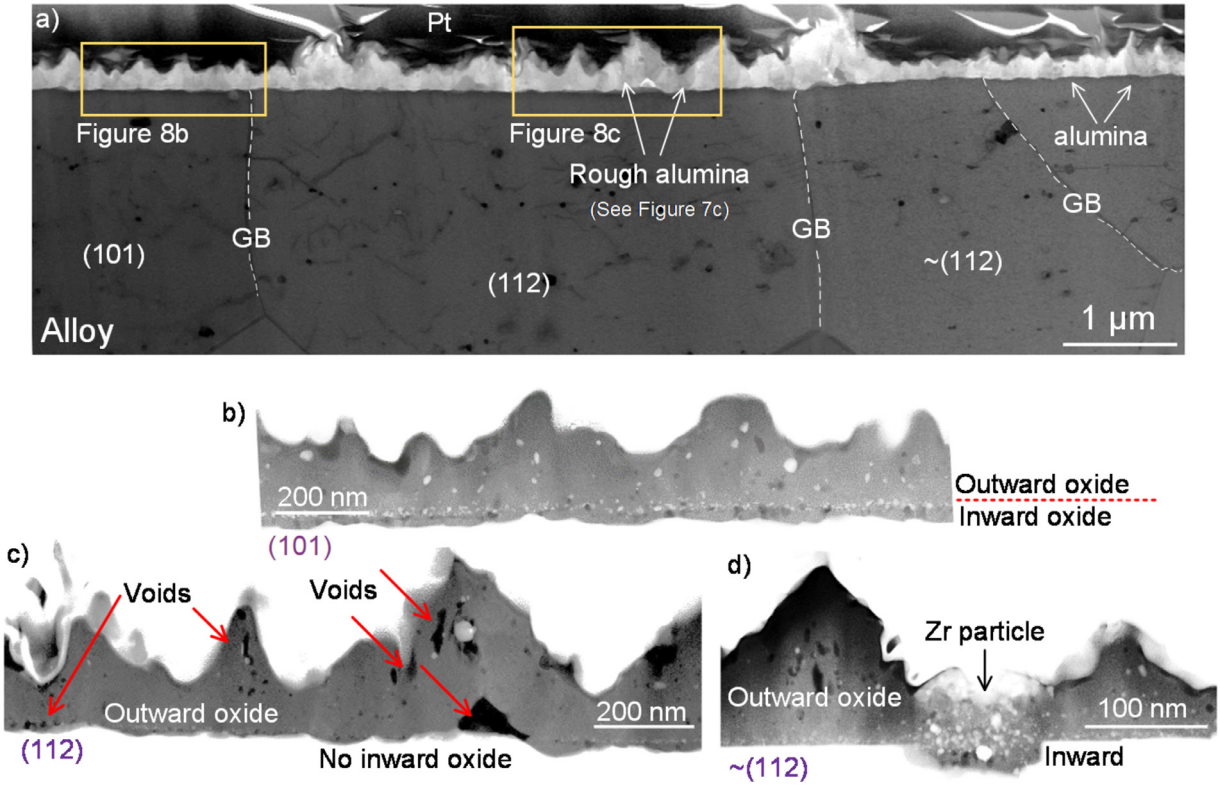

Fig. 8. Detailed morphology of the alumina layer formed on differently oriented grains in the FeCrAl alloy; (*a*) STEM BF cross-section image showing four grains with orientations: (101), (112), close to (112). (*b*) STEM HAADF micrograph showing the microstructure of the alumina layer formed on the (101)-oriented grain. (*c*) High-magnification STEM HAADF image showing the alumina layer microstructure on the (112)-oriented grain. (*d*) STEM HAADF image of the alumina layer on the grain oriented within 5° of (112). The orientation of the grains was determined before exposure. (Exposures in $H_2 + N_2$ + ~35 ppm H_2O for 168 h at 900°C).

the thick scale directly on top of the carbide particle (area 3 in Fig. 9*a*) is rich in magnesium. Based on a combination of TKD analysis and STEM-EDXS analysis (12.5 Mg, 30.3 Al, and 54.5 O (in at. %)) it was concluded that the latter consists of a $MgAl_2O_4$ spinel.

3.6. Failure mode III: The dual role of RE-rich particles in FeCrAl and FeCrNiAl alloys

As demonstrated above (Figs. 8 and 9), exposure to the nitriding gas at 900°C resulted in the formation of a 200 – 400 nm α-alumina scale on the alloy surface. The alumina scale incorporated a high density of alumina pegs [32–36], also referred to as oxide nodules [19], of different sizes all featuring RE (here Y and/or Zr)-rich cores. The density, size, composition, and distribution of the oxide pegs mirrored those of the RE particles in the alloy, revealing that the oxide pegs correspond to RE particles at the alloy surface that have become fully oxidized and incorporated into the alumina scale. There were very few large oxide pegs (one is shown in Fig. 10*a*), mirroring the equally scarce large Y-rich particles in the alloy (Fig. 1*e*).

The RE-containing alumina pegs share several characteristics: (*i*) the peg periphery is pore free and fast growing relative to the base oxide (Fig. 10*b*), and it consists of a nanogranular alumina, which contains relatively high concentrations of RE ions. In this case, the nanograins are decorated with a Y^{3+} layer of atomic thickness, which creates a spiderweb pattern in STEM imaging (Fig. 10*c*), (*ii*) the oxide pegs are multiphase, comprising amorphous alumina regions together with θ- and α-alumina grains and scattered YAG ($Y_3Al_5O_{12}$) nanoparticles [19] (Fig. 10*c*), and (*iii*) the RE gradient in the peg indicates that RE ions (Y^{3+} in Fig. 10*b*) are transported toward the scale/alloy interface. As noted in [19], the latter observation (confirmed by STEM-EDXS) contradicts the classical oxidation scenario where cations migrate towards a cathode situated at the scale/gas interface.

The base alumina layer was further studied to explore the fate of the nanosized Y- or Z-rich particles in the alloy (~6 particles/µm^3). In the example in Fig. 11*a*, a small oxide peg corresponding to a nanosized Zr-rich particle is shown. Investigation using STEM-EDXS showed that the oxide pegs forming at the nanosized Zr particles are similar to the large alumina peg in Fig. 10*a–c*, *i.e.*, featuring a RE-rich core and a nanogranular multiphase alumina periphery with RE ion- (Zr^{4+} here) decorated nanograin boundaries. The unique properties of the alumina pegs are thus independent of both size and composition, *e.g.* whether they contain Y (Fig. 10) or Zr (Fig. 11*a*). In addition, compositional analysis of the base alumina layer using STEM-EDXS (not shown) revealed that it contained Y or Zr ions only at sites where the nanosized RE-bearing oxide pegs had become incorporated into it. This is in accordance with the recent finding [19] that REs in FeCrAl Kanthal APMT are solely present in particulate form.

In a previous study using similar exposure conditions it was revealed that water penetrates the interfaces of Y- or Zr decorated nano-granular alumina pegs [19]. To study this effect further, TOF-SIMS surface mapping and depth profiling were carried out on a FeCrAl-sample that had been exposed to a nitriding environment where H_2 was replaced by D_2, forming D_2O with the traces of O_2 in the hot gas. Analysis of the alloy surface (Fig. 11*b*) revealed several relatively large oxide pegs that were all enriched in Y. Importantly, deuterium was detected in the Y-rich pegs and only there. Moreover, depth profiling of micro- and nano-sized Y-rich alumina pegs (see Fig. 11*b* and *c*) revealed that they all contained deuterium. The deuterium concentration profile in the oxide pegs was similar to that of Y, with the exception of a deuterium pile-up

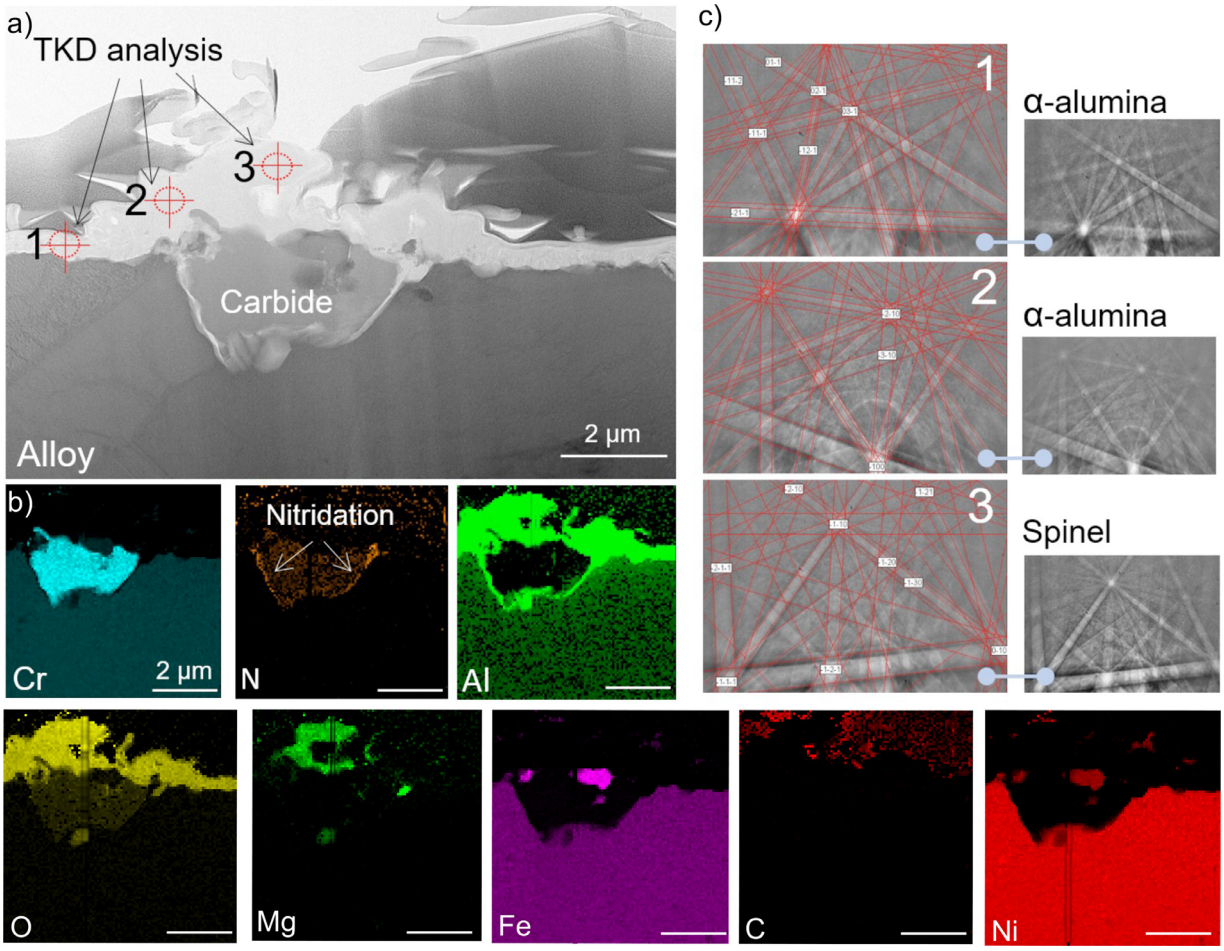

Fig. 9. Effect of carbide particles on the nitridation of the FeNiCrAl alloy. (*a*) STEM BF micrograph showing a $M_{23}C_6$ carbide particle at the alloy surface after the exposure. It is covered by a relatively thick alumina scale, (*b*) STEM-EDXS analysis showing the formation of AlN at the alloy/particle phase boundary, and (*c*) SEM-TKD diffraction patterns acquired from three locations in the alumina scale (*a*) demonstrating the presence of a spinel region directly on top of the carbide particle. ($H_2 + N_2$ + ~3 ppm H_2O for 168 h at 900°C).

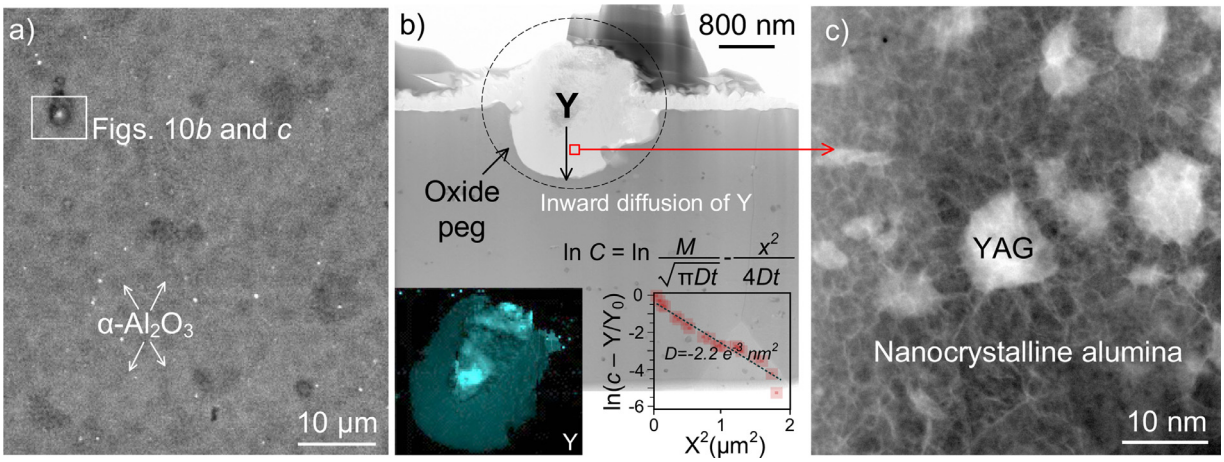

Fig. 10. Incorporation of Y-rich particles into the oxide scale on the FeCrAl alloy. (*a*) SEM backscattered electron image of the alloy surface after the exposure (the boxed area relates to the analyses in Figs. 10*b* and *c*), (*b*) STEM BF image showing a cross-section from the boxed area in Fig. 10*a*, which includes a large (2 μm) oxide (alumina) peg formed around a Y-rich inclusion, STEM-EDXS of the cross section showing the Y map (O and Al are not shown), and the logarithmic plot obtained by EDXS line scan and the approximate solution to Fick's second law showing a logarithmic Y-concentration trend in the alumina nodule, and (*c*) high-resolution STEM HAADF micrograph showing a network pattern (5–30 nm) in the oxide nodule corresponding to Y-decorated alumina nanograins, as confirmed by STEM EDXS, and electron energy loss spectroscopy. Note: The oxidized specimen studied in a previous paper [19] was further investigated here.

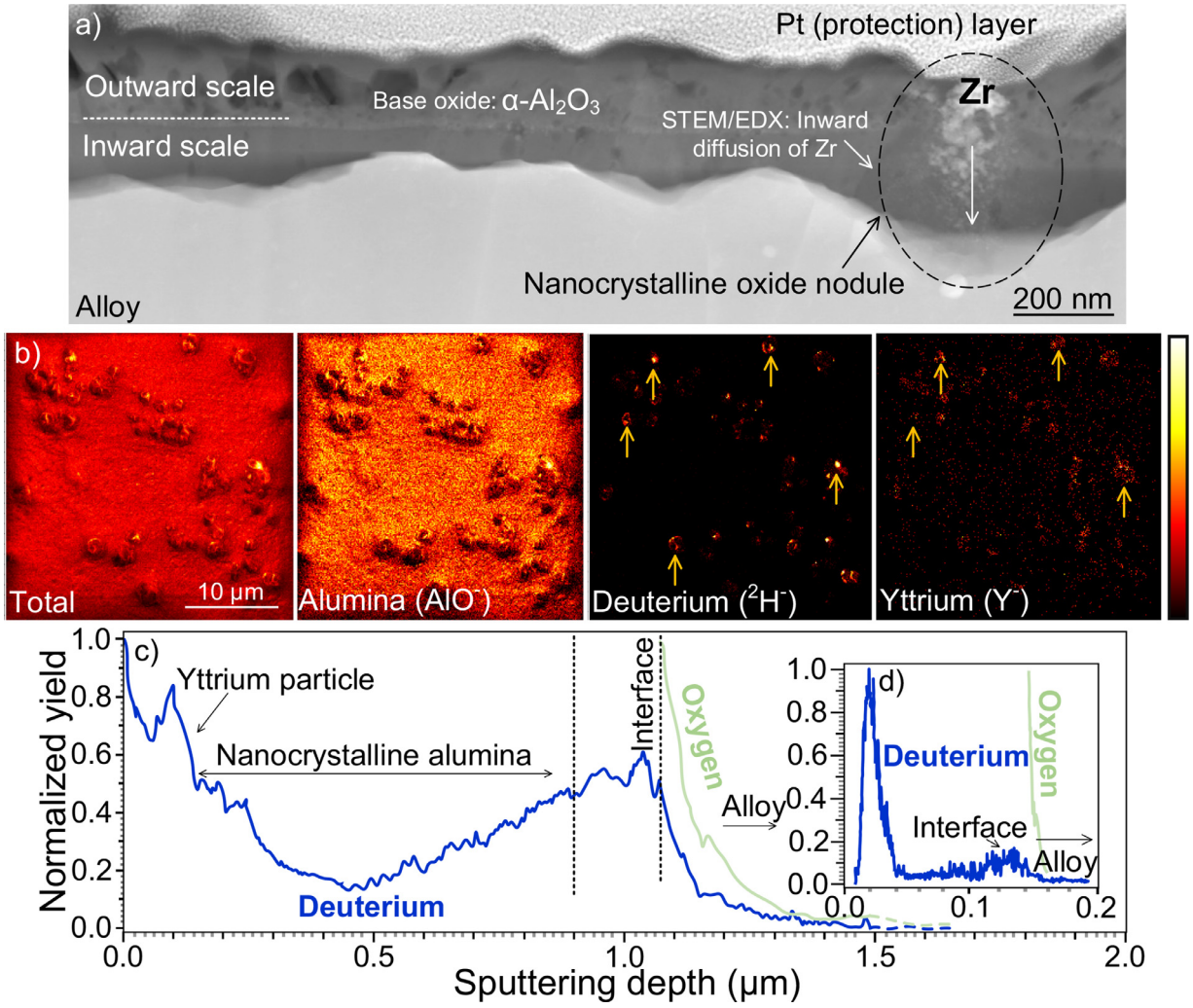

Fig. 11. Formation of the oxide scale via cooperation of REs and water on the FeCrAl alloy. (*a*) STEM HAADF image showing the incorporation of a *nanosized* RE (Zr) particle into the alumina scale, (*b*) TOF-SIMS 2D surface mapping of a sample exposed to N_2 + D_2 showing the distribution of Y and D on the surface of the alumina scale (the arrows indicate the co-occurrence of Y and D), (*c* and *d*) TOF-SIMS depth profiles of micro- and *nanosized* pegs in the alumina scale. The scale/alloy interfaces correspond to the rapidly decreasing oxygen signals. (Exposures to $H_2 + N_2$ + ~35 ppm H_2O and to $D_2 + N_2$ + ~35 ppm D_2O for 168 h at 900°C).

observed at the alloy/oxide interface. It was also noted that the base alumina layer did not contain significant amounts of D (not shown). The Zr –rich oxide pegs were too small for analysis using TOF-SIMS.

In order to investigate the role of Zr- and Y-rich particles of varying sizes on nitridation, cross-sectional analysis using SEM-EDXS and STEM-EDXS was performed on a large number of alumina pegs forming upon exposure of the FeCrAl to the nitriding environment at 900°C (Fig. 12). As indicated above, Y and Zr particles < 150 nm are omnipresent in the FeCrAl (Fig. 1*e*). Such nanosized Zr and Y particles become completely embedded in the base alumina layer upon oxidation (Fig. 10*a*). In contrast, the small number of large alumina pegs were accompanied by cracks and pores at the interface between the base alumina layer and the pegs (Fig. 12*a*). Notably, the alloy substrate beneath these scale imperfections often suffered nitridation (see the representative examples in Figs. 3*b* and 12*a*). A similar relationship between the size of Y- and Zr-rich particles and the defects in the alumina scale in the vicinity of the alumina pegs was also evident in oxygen-rich environments (see Fig. 12*b*).

4. Discussion

The results show that the two FeCrAl and FeNiCrAl alumina-forming alloys studied exhibit similar morphologies of nitridation. The highly localized nature of corrosion implies that the nitridation can be attributed to cracks and other imperfections in the thermally grown alumina scale, which allow the nitriding gas to come into direct contact with the alloy; the alumina layer itself being, in principle, impermeable by nitrogen. A previous study by Geers et al. [17] proposed that the presence of chromia domains in an otherwise defect-free and continuous alumina scale can cause nitridation. Using a combination of first principles calculations and thermodynamic considerations, the authors showed that Cr_2O_3 scales on Al-containing alloys are expected to be permeable to nitrogen at high temperatures. The formation of defect-rich metastable chromium oxy-nitrides was reported to provide diffusion paths for nitride ions across the scale.

The present study takes a fresh look at the nitridation of alloys by characterizing the scale imperfections that cause nitridation and investigating how they are related to alloy microstructure. Three

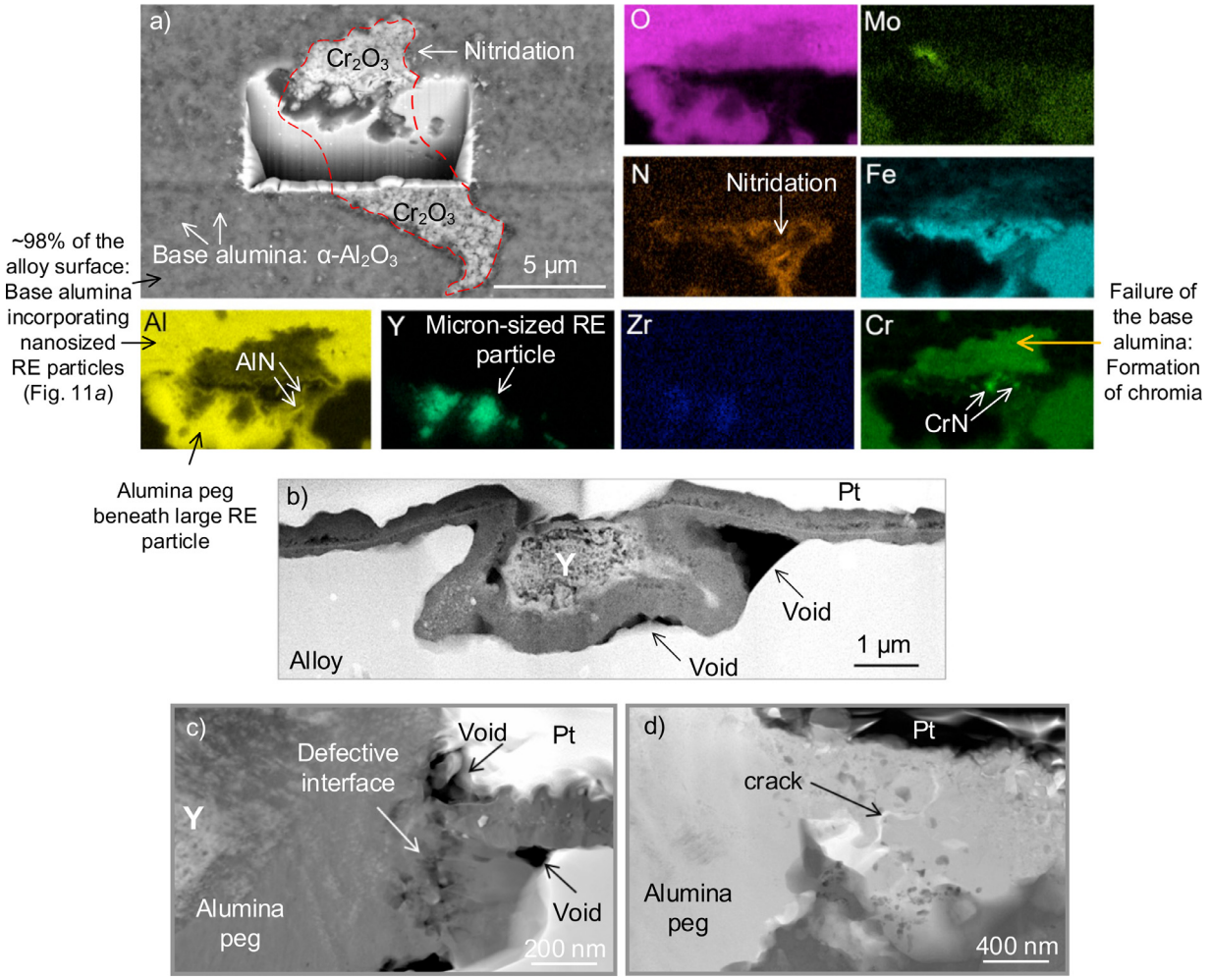

Fig. 12. Investigating the oxidation morphology at micron-sized Y- and/or Zr-rich particles in the FeCrAl alloy exposed to two different environments. (*a*) FIB-SEM-EDXS analysis revealing nitridation in the vicinity of a micron-sized RE-rich particle, (*b-d*) FIB-STEM analysis showing the formation of voids at the fast-growing alumina/base alumina/alloy interfaces. Note: (*a, c,* and *d)* are from the FeCrAl alloy exposed to $H_2 + N_2$ + ~35 ppm H_2O for 168 h at 900°C, whereas (*b*) is from the alloy exposed in oxidizing environment, *i.e.,* 20% H_2O + O_2 for 168 h at 900°C.

distinct modes of alumina scale failure were identified that provide pathways for nitrogen across the scale: (a) poorly protective alumina barrier layers forming on alloy grains having a specific crystallographic orientation, (b) chromium carbide precipitates, and (c) micrometer-sized RE-rich precipitates that cause cracks and pores in the scale. It is emphasized that the microstructural characterization of "scale failure modes" (b) and (c) correspond to the early stages of nitridation which, with time, develop into the characteristic nitrided zones shown in Figs. 2–5.

The formation of open cracks that penetrate the alumina scale enables N_2 (g) to reach the bare alloy surface where the nitrogen molecules can dissociate and dissolve into the metal. However, in, e.g., air or in N_2-containing gases with high concentrations of water vapour, a new barrier alumina layer tends to form rapidly on the metal exposed in the crack. This is because oxygen outcompetes nitrogen for aluminium, forming an alumina layer on the metal surface. Thus, alumina is thermodynamically strongly favoured over aluminium nitride, e.g., ΔG for the reaction:

$$2AlN(s) + 3H_2O(g) \rightarrow Al_2O_3(s) + N_2(g) + 3H_2(g) \quad (1)$$

is -371.83 kJ/mol Al_2O_3 at 900°C (calculated by Factsage 7.3 [37]) ($K = 2.56 \times 10^{15}$), meaning that even in the strongly nitriding atmosphere used in this study, AlN spontaneously forms alumina. However, if the concentration of the oxygen-carrying molecule (H_2O in this case) is low and/or if the transport paths are narrow, the rate of oxygen uptake by the metal surface may become limited by gas phase transport of H_2O, allowing N_2 (having much higher concentration) to dissolve into the alloy and form AlN. Importantly, AlN precipitation depletes the alloy in aluminium and, thus, disallows crack healing by formation of a new barrier alumina layer. The experimental conditions in the present study (900°C, $p(N_2) = 0.95$ bar, $p(H_2) = 0.05$ bar, $pH_2O = 35$ ppm), is an example of the latter situation, i.e., even though the reaction (Eq. 1) is spontaneous in the gas, AlN is observed beneath cracks in the alumina scale. The relative thermodynamic stability of alumina compared to AlN is illustrated in Fig. 5*b*, a comparison of the O and N maps showing that the AlN precipitates in the alloy are partly converted to oxide. The importance of scale cracks for nitridation of alumina-forming alloys is in accordance with the findings of Han et al. [38]. They subjected a Ni-based alloy to cyclic exposure in lab air at 1100°C and observed that the extent of nitridation increased with the number of thermal cycles and attributed this to increased cracking of the alumina scale.

The current study of the alumina scales formed on two alloys identifies three distinct failure modes which allow nitrogen to penetrate and cause alloy nitridation. While the thermodynamic driving force is the same and the phases appearing are similar, each failure mode is associated with a characteristic morphology of nitridation.

4.1. Failure mode I: Orientation-dependent oxidation and nitridation

The "marker" experiments on the FeCrAl alloy reveal that scale morphology and the susceptibility towards nitridation are both related to the crystallographic orientation of the alloy grains. It may be noted that the overwhelming majority of grains formed a relatively even and defect-free alumina scale, exhibiting the typical duplex (inward-outward) layer morphology [39–41] (morphology *i*, see Figs. 2*a-c*, 7*b*, 8*b*). In contrast, a small fraction of the grains formed thick, porous and very uneven scales (morphology *ii*, see Fig. 8*c* and *d*). Similar "rough" alumina scales have been reported to form on FeCrAl alloys in this temperature range and have been attributed to outward-growing metastable aluminas (e.g., γ-Al_2O_3) [41–43]. Also, the metastable alumina in the "rough" scale is reportedly transformed to α-Al_2O_3 with time [44,45]. Accordingly, the present finding that the "rough" scale consists of α-Al_2O_3 is attributed to the transformation of an originally formed metastable alumina to α-Al_2O_3 during the course of the 24 h exposure at 900°C. The "marker" experiments clearly show that only bcc grains with (112)- and close to (111)- oriented surfaces develop the "rough" morphology. Hence, it is proposed that alloy grains with those orientations are less favourable for α-Al_2O_3 formation, and therefore more likely to support the formation of a relatively fast-growing metastable alumina scale under the experimental conditions.

A somewhat similar dependence of alumina scale growth on the crystallographic orientation of the bcc substrate was reported by Tolpygo and Clarke [46]. Investigating the initial oxidation of FeCrAl alloy single-crystals at 1000°C, they observed undulations in the α-alumina scales which were more pronounced on (111) orientated grains than on (100)- and (110)- oriented surfaces, resulting in faster relaxation of scale growth stresses on the (111) grains. Moreover, investigating the influence of grain orientation on the formation of alumina on the ODS single-crystal FeCrAl Incoloy MA956 at 800 and 1000°C, Tyagi et al. [47] reported that alumina scales grown on (111) substrates were thicker than scales on (110) substrates. The notion that the characteristics of the transient oxidation of alloys are influenced by substrate orientation has also been reported by Doychak et al. [48], who investigated the early stages of oxide scale formation on β-NiAl alloy single-crystals upon exposure to air at 800 and 1100°C. They showed that metastable alumina polymorphs form epitaxially on crystals with (112) and (111) orientations [48].

In the present study, it is striking that the very same (112) grain orientation that tends to grow a "rough" alumina scale is also the only grain orientation suffering nitridation (see Fig. 7), there being no evidence for nitridation of FeCrAl grains with other orientations, except in the vicinity of carbide particles and large RE-rich precipitates. This indicates that the alumina scale forming on (112)-oriented alloy grains is permeable to nitrogen, while the alumina scale formed on grains with other orientations is not. This, in term, implies that it is the slower establishment of an α-Al_2O_3 layer on the alloy surface which makes the alloy susceptible to nitridation. As mentioned above, the nitrided grains exhibit morphology *iii* (bright contrast in plan view corresponding to a very thin alumina layer, see Figs. 5 and 7) or *iv* (dark contrast in plan view and a thick, rough alumina, see Fig. 7). That grains with orientations supposed to further the formation of a fast-growing metastable alumina scale exhibit very thin alumina layers after nitridation (Fig. 5) may seem counter-intuitive. To resolve this apparent paradox, it is argued that nitridation has started in the early stages of the exposure, at a time when the surface is covered by a thin layer of transient alumina which is permeable to N_2.

A typical example of morphology *iii* is in Fig. 5, showing nitridation of a (112) oriented grain, the scale covering the nitrided zone being much thinner than on the surrounding sound alloy. The absence of large RE-rich particles is notable. The scale consists of three layers; a top alumina layer containing defects and cracks and incorporating CrN and Cr_2N particles; a bottom discontinuous AlN layer; and a middle layer consisting of remaining alloy which is fully Al depleted and partially depleted in Cr. The three-layered scale is suggested to have formed in the following way: Initially, a thin transient alumina layer forms which is permeable to nitrogen. Because the alloy substrate in contact with the alumina layer is Al depleted, the nitrogen dissolving into the alloy must reach deeper into the substrate in order to form aluminium nitride, causing the bottom AlN layer to form. The early ingress of nitrogen and formation of an AlN sub-layer getters Al in the alloy matrix, effectively stopping further growth of the alumina layer. In this scenario, early nitridation thus makes the formation of a protective alumina scale virtually impossible.

In this situation, the flux of nitrogen past the discontinuous AlN layer into the alloy, results in formation of a deep nitrided zone. With time, the AlN layer in the scale is partly converted to oxide (Fig. 5*b*), showing that oxygen has dissolved into the remaining alloy. Also, nitrogen reacts with chromium in the Al-depleted alloy and forms Cr_2N and CrN. With time, the chromium still present in the remaining alloy reacts with water to form chromia. It is suggested that the nitrided grains exhibiting a thick and rough scale (morphology *iv*) are only partially nitrided, allowing alumina growth to continue over part of the grain surface.

An inspection of Fig. 7 shows that the (112) orientated bcc alloy surface which promotes both outward alumina growth and alloy nitridation, features a lower atomic density than other low-index planes, e.g., (100) and (101). This suggests that the atomic surface density influences the early growth of the alumina scale so as to affect both α-alumina formation and the ability of the scale to protect against nitrogen ingress. Further investigation is needed to elucidate the mechanisms behind this trend, e.g., by molecular dynamic simulations of the surface atoms in various crystallographic orientations.

The observation of CrN and Fe-rich alloy particles sitting on top of the alumina scale covering the nitrided zones (Fig. 4) is reminiscent of a paper by Grabke et al. [49] reporting that nitridation of a Ni-Cr alloy in a NH_3-H_2O mixture caused metallic (Ni)-particles to appear on the surface of the nitrided alloy. It was suggested that the volume increase due to internal nitridation was responsible for the formation of the external particles, the resulting "pressure" causing a flux of solid material to the top of the scale. In the present case, the formation of "external" CrN particles is instead attributed to solid state diffusion. The formation of Cr_2N and CrN precipitates in the Al depleted layer beneath the alumina scale is shown in Fig. 5. CrN particles which are in contact with both the gas and the alloy substrate are suggested to grow by an *electrochemical* process similar to the thermal growth of oxide layers:

$$1/2N_2(g) + 3e^- \rightarrow N^{3-}(CrN) \quad \text{At gas/CrN interface} \tag{2}$$

$$Cr(ss) \rightarrow Cr^{3+} + 3e^-(CrN) \quad \text{At alloy/CrN interface} \tag{3}$$

$$Cr(ss) + 1/2N_2(g) \rightarrow CrN(s) \quad \text{Sum reaction} \tag{4}$$

CrN is a rock-salt structured metallic nitride where the Cr^{3+} ions are situated in the octahedral interstices in an fcc arrangement of nitride ions. The small rCr^{3+}/rN^{3-} ratio (= 0.42) implies that it is a cation conductor. Hence, a CrN crystal situated at the alloy gas interface is expected to *grow outward,* explaining why CrN particles appear to sit on the top surface. The appearance of remaining metal on the surface may be due to a local increase in pressure due to chromium nitride growth, according to Grabke [49]. In the presence of N and Cr gradients in the Al depleted metal, CrN crystals that precipitate *beneath* the alloy/gas interface

are also expected to grow outward, towards the surface. This may cause parts of the depleted alloy to become disconnected from the bulk alloy.

4.2. Failure mode II: The effect of carbide precipitates

The quasi-in-situ experiments (*e.g.*, Figs. 7 and 9) give evidence of alloy nitridation at the interface between the alloy and the carbide particles, showing that the alumina scale formed at chromium-rich carbide particles is locally non-protective. While chromium-rich carbide precipitates (i.e., $M_{23}C_6$ and M_7C_3) are common in many high-temperature alloys, including Nikrothal PM58, their influence on the formation of protective oxide scales at high temperatures has not been studied much. The growth of protective alumina scales is expected to be affected by carbide particles because the aluminum needed to form alumina on the particle cannot be provided by diffusion across it, as chromium-rich carbides reportedly do not dissolve aluminum [50,51]. Thus, an alumina scale growing on a carbide particle at the surface must be supplied with aluminum from the surrounding alloy. The results show that the scale at the carbide particles differs from the surrounding base alumina by being significantly thicker and made up of a mixture of α-alumina and $MgAl_2O_4$ spinel, the base oxide only consisting of α-alumina. Concerning the appearance of $MgAl_2O_4$ it may be noted that alumina-forming high-temperature alloys often contain on the order of 100 ppm (by weight) of Mg. Because of the high affinity of Mg for oxygen, Mg^{2+} is enriched in the alumina scale. Also, Mg^{2+} has a relatively high diffusivity in oxide scales, causing it to accumulate at the scale/gas interface. Accordingly, there are several observations of $MgAl_2O_4$ spinel in alumina scales on high-temperature alloys [52]. Similar to Al, there is little evidence for solubility of Mg in chromium-rich carbides. However, Mg has been reported to segregate to the interface between Cr-rich carbide particles and the alloy substrate [53]. Hence, the magnesium source in this case is likely the interface between the carbide inclusion and the alloy.

The mixed spinel/corundum scale on top of the carbide particles is suggested to have formed in the following way: During early oxidation, i.e. during heat-up, the growing scale mainly consists of transient alumina, e.g., γ-Al_2O_3. Due to Mg oxidation, the transient alumina in the vicinity of the carbide particles become heavily doped with Mg^{2+}, i.e., to form γ-$Al_{2-x}Mg_xO_{3-½x}$. (The maximum solubility of divalent cations in γ-Al_2O_3 at 900 °C is close to 20 % (cationic) [54]). Importantly, doping with divalent cations is known to stabilize transient alumina [55]. Hence, the relatively fast-growing transient alumina is expected to transform later in the vicinity of the carbide particles, explaining the relatively thick scale observed at these sites. The spinel/corundum mixture is suggested to have formed according to:

$$\gamma - Al_{2-x}Mg_xO_{3-1/2x} \rightarrow (1 - 3x/2)\alpha - Al_2O_3 + x\,MgAl_2O_4 \qquad (5)$$

as described by Fang et al. [54]. According to the discussion on the substrate orientation effect, transient alumina scales have relatively poor ability to protect against nitrogen ingress. This implies that the alloy is susceptible to nitridation at these locations because the transient alumina is stabilized through Mg^{2+} doping. Also, $MgAl_2O_4$ spinel was observed to be in contact with underlying carbide precipitate (not shown), suggesting that the spinel oxide may play an active role in nitrogen transport across the scale.

4.3. Failure mode III: The dual role of RE-rich particles

The high density of RE-rich nanoparticles in Kanthal APMT (c.f. Fig. 1) is crucial for its excellent oxidation resistance and creep strength at high temperatures [18]. A recent paper has provided new insights into the role of the RE-rich particles and water in the early growth of alumina scales on FeCrAl alloys [19]. A combination of experiment and theory showed that Y and/or Zr enriched alumina pegs enable water to access an inner cathode situated close to the alloy/ peg interface, water penetrating via Y^{3+} (or Zr^{4+})-rich interfaces between alumina nanograins in the pegs.

The present study shows the crucial importance of the size of the Y- and Zr-rich particles for oxidation performance. Thus, nanosized Y- and Zr-rich particles become incorporated into the base alumina and facilitate its inward growth and are beneficial for the oxidation performance of the alloy. In contrast, the relatively few large RE-rich particles (mainly the Y-rich type) cause cracks in the scale which can cause nitridation. The cracks are likely due to the stresses induced by different growth rates of the base alumina and the faster growing alumina pegs. The schematic presented in Fig. 13 summarizes investigations of a large number of alumina pegs formed around RE-rich particles of varying sizes.

A principal finding, based on a large number of cross-section images (see, e.g., Figs. 10–12 and [19]), is that there is a "critical" RE particle size, above which void formation and cracking of the scale occurs (see, *e.g.*, Fig. 12*c* and *d*), decreasing the ability of the alloy to resist nitridation. It is emphasized that the nitridation shown *e.g.*, in Fig. 12 corresponds to early stages of the nitridation

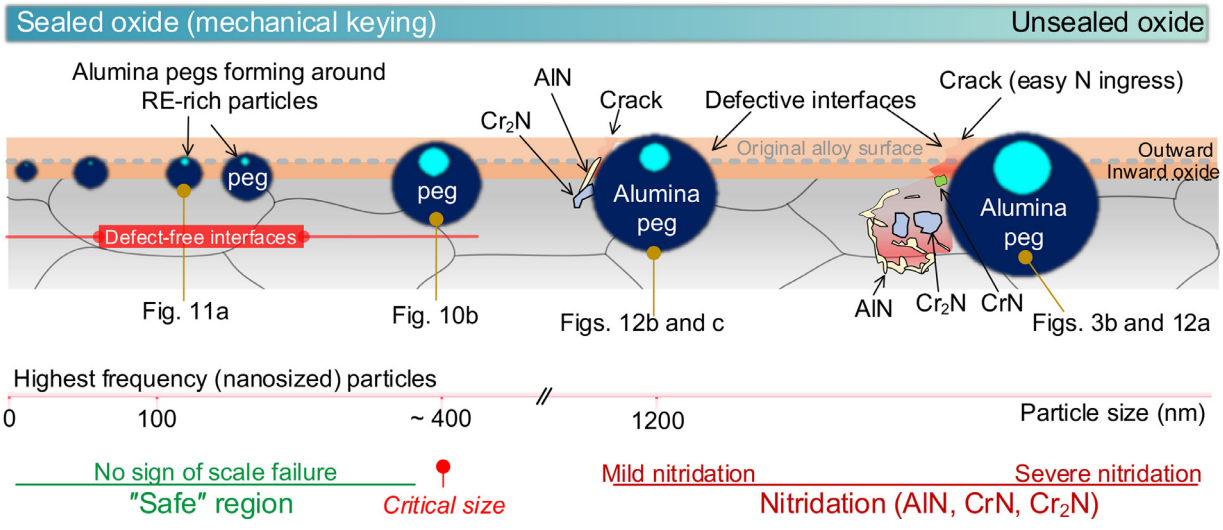

Fig. 13. Schematic illustration indicating how the size of the RE rich particles affects the ability of the alumina scale to protect against nitridation.

process and may develop into the characteristic nitridation morphology in Fig. 3. It is expected that the critical RE particle size depends both on the alloy and on the gas composition and temperature. In the present case, the critical RE particle size for the FeCrAl alloy was ~400 nm.

In early studies of the effect of RE microalloying on the oxidation behaviour of alumina-forming alloys, it was proposed that the characteristic "pegs" in alumina scales formed at large RE particles (often several μm in diameter) were beneficial because of a "mechanical keying" effect which increased scale adhesion [56–58]. On the other hand, it has been noted that large RE-rich oxide particles, resulting from the oxidation of coarse RE particles, cause pores and micro-cracks in the scale, impairing the oxidation properties [59]. The latter interpretation is in accordance with the present observations (Fig. 12), implying that the scale cracks at large oxide pegs serve as channels for N_2, causing alloy nitridation. These observations suggest that oxide scale defects associated with large (mainly Y-rich) RE particles, which make the material susceptible to corrosion, is a feature common to all alumina-forming alloys. Also, the results suggest that the so-called RE overdoping, meaning the detrimental effect on oxidation and corrosion properties of adding too much REs ($\gtrsim$ 0.1 *at.* %) to the alloy is related to RE particle size rather than to the RE concentration.

In summary, by investigating the corrosion of a FeCrAl and a FeNiCrAl alloy in a strongly nitriding environment, the present paper highlights imperfections and weak points in the alumina scales formed. This is first investigation of how the detailed morphology of the alumina scale depends on grain orientation in a polycrystalline alloy and it identifies three modes of scale failure. Each failure mode corresponds to a certain way by which nitrogen can bypass the α-alumina layer which, in itself, appears to be impermeable to nitrogen. While the thermodynamic driving forces are the same and the corrosion products are similar, each failure mode is associated with a characteristic morphology of nitridation. The first failure mode only affects grains in the FeCrAl alloy having certain crystallographic orientations that favour transient, outward-growing aluminas rather than α-alumina. The second mode is connected to Cr-rich carbide precipitates in the alloy where transient alumina growth and $MgAl_2O_4$ formation are promoted by traces of magnesium. The third failure mode involves cracks and pores in the α-alumina scale formed at large oxide pegs which are related to large Y-rich precipitates.

The three modes of failure described may also be relevant for other alloy systems and can inform the development of alloys with superior oxidation properties. Thus, the ability of FeCrAl alloys to withstand nitridation may be improved by controlling the orientation of alloy grains at the surface and by minimizing the number density of large Y-rich particles. For the FeNiCrAl alloy, a similar improvement might be achieved by decreasing the Mg content of the alloy and by minimizing the number density of large Y and Zr-rich particles (detrimental effect of large REs also influences the oxidation behaviour of FeNiCrAl, see *e.g.* Fig. 3*c*).

5. Conclusions

Controlled exposures of two high-temperature FeCrAl and FeNiCrAl alloys in a strongly nitriding environment at 900°C, combined with a quasi-in-situ surface characterization, revealed that nitridation started at imperfections in the alumina scale, the continuous α-alumina scale being impermeable to nitrogen. The principal findings are:

- Nitridation only occurred at specific surface locations and according to three distinct failure modes.
- In the FeCrAl alloy, only grains with (112)- oriented bcc surfaces suffered nitridation, except in the immediate vicinity of large RE-rich precipitates. The same class of (112)- oriented grains also formed a rough, outward-grown scale, originally consisting of transient alumina. The (112) orientated bcc alloy surface features a lower atomic density than other low-index planes, e.g., (100) and (101), suggesting that the atomic surface density influences both the ability to form α-alumina during early growth of the alumina scale and the ability of the scale to protect against nitrogen ingress.
- Inward-grown oxide pegs formed at RE- (yttrium and zirconium) rich inclusions in the FeCrAl and FeNiCrAl alloys. RE-rich particles larger than a "critical" size give rise to correspondingly large oxide pegs that were associated with voids and cracks in the alumina scale, making the alloy susceptible to nitridation.
- The FeNiCrAl alloy suffered nitridation at chromium-rich carbide precipitates, and the alumina scale formed at the particles was outward grown. The susceptibility of these sites for nitridation is attributed to stabilization of transient alumina through Mg^{2+} doping.

Declaration of Competing Interest

The authors declare that they have no known competing financial interests or personal relationships that could have appeared to influence the work reported in this paper.

Acknowledgement

The authors cordially thank Professor David R. Clarke in John A. Paulson School of Engineering and Applied Sciences at Harvard University for his support during this project and the valuable feedback on the manuscript. The authors would also like to thank Dr. Per Malmberg for the SIMS analysis and Dr. Gustav Sundell for helping in the microscopy part of the research. A.N.M. and M.E. greatly acknowledge the Swedish Research Council and the Royal Swedish Academy of Engineering for financial support. This work was carried out at the Swedish High Temperature Corrosion Centre (HTC) at Chalmers University of Technology. The Swedish Energy Agency, AB Sandvik Materials Technology, Kanthal AB and Entech Energiteknik are gratefully acknowledged. This work was also performed in part at the Chalmers Materials Analysis Laboratory (CMAL) and the Monash Centre for Electron Microscopy (MCEM).

Supplementary materials

Supplementary material associated with this article can be found, in the online version, at doi:10.1016/j.actamat.2020.09.058.

References

[1] B.A. Pint, High Temperature Corrosion of Alumina-forming Iron, Nickel and Cobalt-base Alloys, in: B. Cottis, M. Graham, R. Lindsay, S. Lyon, T. Richardson, D. Scantlebury, H. Stott (Eds.), Shreir's Corrosion, Fourth ed., 2010, pp. 606-645.
[2] B. Jonsson, A. Westerlund, Oxidation comparison of alumina-forming and chromia-forming commercial alloys at 1100 and 1200 C, Oxid. Met. 88 (2017) 315–326.
[3] F.H. Stott, G.C. Wood, M.G. Hobby, A comparison of oxidation behavior of Fe–Cr–Al, Ni–Cr–Al, and Co–Cr–Al alloys, Oxid. Met. 3 (1971) 103–113.
[4] F.H. Stott, G.C. Wood, The mechanism of oxidation of Ni–Cr–Al alloys at 1000°–1200°C, Corros. Sci. 11 (1971) 799–812.
[5] I.A. Kvernes, P. Kofstad, Oxidation behavior of some Ni–Cr–Al alloys at hight temperatures, Metall. Trans. 3 (1972) 1511–1519.
[6] A. Chyrkin, N. Mortazavi, M. Halvarsson, D. Grüner, W.J. Quadakkers, Effect of thermal cycling on protective properties of alumina scale grown on thin Haynes 214 foil, Corros. Sci. 98 (2015) 688–698.
[7] G.W. Meetham, High-temperature materials – a general review, J, Mater. Sci. 26 (1991) 853–860.
[8] D. Young, High Temperature Oxidation and Corrosion of Metals, Elsevier, Amsterdam, 2016.
[9] N. Birks, G.H. Meier, F.S. Pettit, Introduction to the High-Temperature Oxidation of Metals, Second ed., Cambridge Univ. Press, Cambridge, 2006.

[10] M.N. Task, B. Gleeson, F.S. Pettit, G.H. Meier, The effect of microstructure on the type II hot corrosion of Ni-base MCrAlY alloys, Oxid. Met. 80 (2013) 125–146.
[11] A.H. Heuer, D.B. Hovis, J.L. Smialek, B. Gleeson, Alumina scale formation: a new perspective, J. Am. Ceram. Soc. 94 (2011) 2698-2698.
[12] T. Gheno, B.C. Zhou, A. Ross, X. Liu, G. Lindwall, Z.K. Liu, B. Gleeson, A thermodynamic approach to guide reactive element doping: Hf additions to NiCrAl, Oxid. Met. 87 (2017) 297–310.
[13] D.P. Whittle, J. Stringer, Improvements in high temperature oxidation resistance by additions of reactive elements or oxide dispersions, Philos. Trans. R. Soc. Lond. B 295 (1980) 309–329.
[14] J. Stringer, The reactive element effect in high-temperature corrosion, Mater. Sci. Eng. A 120 (1989) 129–137.
[15] B.A. Pint, Optimization of reactive-element additions to improve oxidation performance of alumina-forming alloys, J, Ceram. Soc. 86 (2003) 686–695.
[16] D. Naumenko, B.A. Pint, W.J. Quadakkers, Current thoughts on reactive element effects in alumina-forming systems: In memory of John Stringer, Oxid. Met. 86 (2016) 1–43.
[17] C. Geers, V. Babic, N. Mortazavi, M. Halvarsson, B. Jönsson, L.G. Johansson, I. Panas, J.E. Svensson, Properties of alumina/chromia scales in N_2-containing low oxygen activity environment investigated by experiment and theory, Oxid. Met. 87 (2017) 321–332.
[18] B. Jönsson, R. Berglund, J. Magnusson, P. Henning, M. Hättestrand, High temperature properties of a new powder metallurgical FeCrAl alloy, Mater. Sci. Forum 461-464 (2004) 455–462.
[19] N. Mortazavi, C. Geers, M. Esmaily, V. Babic, M. Sattari, K. Lindgren, P. Malmberg, B. Jönsson, M. Halvarsson, J.E. Svesson, I. Panas, L.G. Johansson, Interplay of water and reactive elements in oxidation of alumina-forming alloys, Nat. Mater. 17 (2018) 610–617.
[20] N. Mortazavi, M. Esmaily, M. Halvarsson, The capability of transmission Kikuchi diffraction technique for characterizing nanograined oxide scales formed on a FeCrAl stainless steel, Mater. Lett. 147 (2015) 42–45.
[21] R. Elger, H. Magnusson, K. Frisk, Modelling internal nitridation in an alumina–forming austenitic stainless steel, Mater. Corros. 68 (2017) 143–150.
[22] M. Udyavar, D.J. Young, Precipitate morphologies and growth kinetics in the internal carburisation and nitridation of Fe-Ni-Cr alloys, Corros. Sci. 42 (2000) 861–883.
[23] Data from NIST Standard Reference Database 69. NIST Chemistry Webbook, 2016.
[24] I.I. Gorshkov, A.N. Popandopulo, Structure and properties of modified high-speed steel EP658, Tr. Leningr. Politekh. Inst. 353 (1976) 40–42.
[25] A.N. Popandopulo, L.T. Zhukova, Effect of nitrogen on the stabilization of austenite in a tungsten-molybdenum high-speed steel, Met. Sci. Heat Treat. 27 (1985) 838–840.
[26] R.P. Reed, Nitrogen in austenite stainless steels, JOM 41 (1989) 16–21.
[27] M.O. Speidel, R.M. Pedrazzoli, High nitrogen stainless steels in chloride solutions, Mater. Perform. 31 (1992) 59–61.
[28] J.A. Hawk, J.W. Simmons, J.C. Raviers, Effect of nitrogen alloying on the microstructure and abrasive wear of stainless steels, J, Mater. Eng. Perform. 3 (1994) 259–272.
[29] B. Yang, M.P. Brady, J.A.Turner H.Wang, K.L. More, D.J. Young, P.F. Tortorelli, E.A. Payzant, L.R. Walker, Protective nitride formation on stainless steel alloys for proton exchange membrane fuel cell bipolar plates, J, Power Sources 174 (2007) 228–236.
[30] F. Liu, M. Halvarsson, K. Hellström, J.E. Svensson, L.G. Johansson, First three-dimensional atomic resolution investigation of thermally grown oxide on a FeCrAl Alloy, Oxid. Met. 83 (2015) 441–451.
[31] K. Kuo, Carbides in chromium, molybdenum and tungsten steels, J, Iron Steel Inst 173 (1953) 363–375.
[32] B. Lustman, The intermittent oxidation of some nickel-chromium base alloys, JOM 2 (1950) 995–996.
[33] C.S. Giggins, F.S. Pettit, The oxidation of TD NiC (Ni-20Cr-2 vol pct ThO_2) between 900° and 1200°C, Met. Trans. 2 (1971) 1071–1078.
[34] J. Stringer, I.M. Allam, D.P. Whittle, The high temperature oxidation of Co-Cr-Al alloys containing yttrium or hafnium additions, Thin Solid Films 45 (1977) 377–384.
[35] I.M. Allam, D.P. Whittle, J. Stringer, Improvements in oxidation resistance by dispersed oxide addition: Al_2O_3-forming alloys, Oxid. Met. 13 (1979) 381–401.
[36] R. Pendse, J. Stringer, The influence of alloy microstructure on the oxide peg morphologies in a Co-10% Cr-11%Al alloy with and without reactive element additions, Oxid. Met. 23 (1985) 1–16.
[37] C.W. Bale, E. Bélisle, P. Chartrand, S.A. Decterov, G. Eriksson, A.E. Gheribi, K. Hack, I.H. Jung, Y.B. Kang, J. Melançon, A.D. Pelton, S. Petersen, C. Robelin, J. Sangster and M-A. Van Ende, FactSage Thermochemical Software and Databases, 2010-2016, Calphad 54 (2016) 35–53.
[38] S. Han, D.J. Young, Oxidation - nitridation of Ni-Cr-Al alloys, Mat. Res. 7 (2004) 11–16.
[39] P.Y. Hou, Oxidation of Metals and Alloys, in: B. Cottis, M. Graham, R. Lindsay, S. Lyon, T. Richardson, D. Scantlebury, H. Stott (Eds.), Shreir's Corrosion, Fourth ed., 2010, pp. 195-239.
[40] W.J. Quadakkers, A. Elschner, W. Speier, H. Nickel, Composition and growth mechanisms of alumina scales on FeCrAl-based alloys determined by SNMS, Appl. Surf. Sci. 52 (1991) 271–287.
[41] K. Hellström, N. Israelsson, N. Mortazavi, S. Canovic, M. Halvarsson, J.E. Svensson, L.G. Johansson, Oxidation of a dispersion-strengthened powder metallurgical FeCrAl alloy in the presence of O_2 at 1,100°C: the influence of water vapour, Oxid. Met. 83 (2015) 533–558.
[42] S. Chevalier, A. Galerie, O. Heintz, R. Chassagnon, A. Crisci, Thermal alumina scales on FeCrAl: characterization and growth mechanism, Mater. Sci. Forum 595-598 (2008) 915–922.
[43] K. Reszka, J. Morgiel, Z. Zurek, A. Jaron, Characterization of alumina scale formed on FeCrAl steel, Arch. Metall. Mater. 59 (2014) 77–81.
[44] J. Engkvist, S. Canovic, K. Hellström, A. Järdnäs, J.E. Svensson, L.G. Johansson, M. Halvarsson, Alumina scale formation on a powder metallurgical FeCrAl alloy (Kanthal APMT) at 900–1,100°C in dry O_2 and in O_2 + H_2O, Oxid. Met. 73 (2010) 233–253.
[45] A.Stierle Vlad, N. Kasper, H. Dosch, M. Rühle, In situ x-ray study of the γ- to α-Al_2O_3 phase transformation during atmospheric pressure oxidation of NiAl(110), J, Mater. Res. 21 (2006) 3047–3057.
[46] V.K. Tolpygo, D.R. Clarke, Wrinkling of α-alumina films grown by thermal oxidation – I. Quantitative studies on single crystals of Fe-Cr-Al alloy, Acta Mater 46 (1998) 5153–5166.
[47] A.K. Tyagi, K. Szot, A. Czyrska-Filemonowicz, D. Naumenko, W.J. Quadakkers, Significance of crystallographic grain orientation for oxide scale formation on FeCrAl ODS alloys studied by AFM and MCs+-SIMS, Mater. High Temp. 17 (2000) 159–163.
[48] J. Doychak, J.L. Smialek, T.E. Mitchell, Transient oxidation of single-crystal B–NiAl, Metall. Mater. Trans. A 20 (1989) 499–518.
[49] H.J. Grabke, S. Strauss, D. Vogel, Nitridation in NH_3-H_2O-mixtures, Mater. Corros. 54 (2003) 895–901.
[50] K.O.E. Henriksson, N. Sandberg, J. Wallenius, Carbides in stainless steels: results from ab initio investigations, Appl. Phys. Lett. 93 (2008) 191912.
[51] L.P. Villars, L.D. Calvert, W.B. Pearson, Pearson's Handbook of Crystallographic Data for Intermetallic Phases, American Society for Metals, Metal Park, Ohio (1985).
[52] F. Liu, H. Götlind, J. Svensson, L.G. Johansson, M. Halvarsson, TEM Investigation of the microstructure of the scale formed on a FeCrAlRE alloy at 900°C: the effect of Y-rich RE particles, Oxid. Met. 74 (2010) 11–32.
[53] H.L. Ge, W.V. Youdelis, G.L. Chen, Effect of interfacial segregation of magnesium on high carbon (18%Cr) cast steel, Mater. Sci. Technol. 5 (1989) 1207–1211.
[54] F. Liu, H. Götlind, J.E. Svensson, L.G. Johansson, M. Halvarsson, Early stages of the oxidation of a FeCrAlRE alloy (Kanthal AF) at 900°C: A detailed microstructural investigation, Corros. Sci. 50 (2008) 2272–2281.
[55] M. Kusunoki, M. Rokkaku, Y. Ikuhara, H. Yanagida, TEM study on stability of Mg-doped gamma alumina fine particles, Mater. Trans. JIM. 39 (1998) 110–113.
[56] R. Pendse, J. Stringer, The influence of alloy microstructure on the oxide peg morphologies in a Co-10% Cr-11%Al alloy with and without reactive element additions, Oxid. Met. 23 (1985) 1–16.
[57] H. Hindam, D. Whittle, Peg formation by short-circuit diffusion in Al_2O_3 scales containing oxide dispersions, J, Electrochem. Soc. 129 (1982) 1147–1149.
[58] J. Nowok, Formation mechanisms of keying or pegging yttrium oxide and increased plasticity of alumina scale on FeCrAlY, Oxid. Met. 18 (1982) 1–17.
[59] W.J. Quadakkers, L. Singheiser, Practical aspects of the reactive element effect, Mater. Sci. Forum. 369–372 (2001) 77–92.